Received: 12 April 2020 | Revised: 13 July 2020 | Accepted: 14 July 2020

DOI: 10.1111/ffe.13312

ORIGINAL CONTRIBUTION

FFEMS Fatigue & Fracture of Engineering Materials & Structures WILEY

The influence of microstructure on the fatigue crack growth rate in marine steels in the Paris Region

Victor Igwemezie[1,2] | **Ali Mehmanparast**[1] | **Feargal Brennan**[3]

[1]Offshore Energy Engineering Centre, Cranfield University, Cranfield, UK

[2]Materials and Metallurgical Engineering Department, Federal University of Technology, Owerri, Nigeria

[3]Naval Architecture, Ocean & Marine Engineering Department, University of Strathclyde, Glasgow, UK

Correspondence
Victor Igwemezie, Offshore Energy Engineering Centre, Cranfield University, Cranfield, UK.
Email: victor.igwemezie@structuralintegrity.eu

Funding information
UK Engineering and Physical Sciences Research Council (EPSRC), Grant/Award Number: EP/L016303/1

Abstract

This paper presents a study on the effect of microstructure on the fatigue crack growth (FCG) rate in advanced S355 marine steels in the Paris Region of the *da/dN* versus ΔK log–log plot. The environments of study were air and seawater (SW), under constant amplitude sinewave fatigue loading. Fundamentally, three phenomena (crack tip diversion, crack front bifurcation and metal crumb formation) were observed to influence the rate of FCG. These phenomena appear to be a function of the material microstructure, environment and crack tip loading conditions. The three factors retarded the crack growth by reducing or redistributing the effective driving force at the main active crack tip. A crack path containing extensively the three phenomena was observed to offer strong resistance to FCG. In SW, the degree of the electrochemical dissolution of the *microplastic zone* appears to be an additional primary factor influencing FCG in the steels.

KEYWORDS

corrosion fatigue, crack path, crack tip blunting, microstructure, Paris Region, S355 steel

1 | INTRODUCTION

Understanding how a crack propagates in a given material is fundamental to all forms of theoretical postulations, modelling, analytical and numerical analyses. If the premise of crack growth path is wrong, no matter how elegant the mathematical or numerical expression may appear, the result will not represent reality. The knowledge of corrosion fatigue and its mechanism is of immense value in preventing failure in marine environment. Understanding the influence of microstructure on fatigue mechanism is fundamental because it supports fatigue life prediction of structures, design of fatigue-resistant materials and realistic fatigue modelling attempts. Fatigue is a complex problem and there have been several numbers of publications on the problem of fatigue, each presenting similar or different ideas or trying to modify existing theories—using from simple to complex analytical and numerical approaches. Generally, fatigue crack growth (FCG) in metallic materials is divided into three regions. Each region has been reported to exhibit different mechanisms and characteristics. These regions are the threshold region (or early stages of fatigue crack development), the Paris Region (or the linear and steady crack growth stage) and region of final failure (or unstable/accelerated crack growth stage). The Paris Region is of interest in this study because it is the part commonly used and recommended in ASTM E647-15[1] and BS EN ISO 11782-2:2008[2] for engineering design.

In many reports,[3–10] microstructure, mean stress, residual stress, mechanical properties and initial crack

length were said to have large influence on the threshold and final failure regions. In addition, the accelerated region is said to be influenced by sample thickness. These factors were reported to have little or negligible effects when the propagating crack has grown to a considerable length or beyond few grains, usually in the Paris Region.[5,11–16] In the threshold region, non-continuum or single shear mechanism is said to operate and the nature of the fractured surface is seen to be faceted. The crack tip was under both tensile and shear forces. The crack closure phenomenon was reported to be high and the plastic zone size is equal or less than the microstructural grain diameter. In the final or accelerated failure region, fatigue and additional static loading modes are said to operate. Also, microvoid coalescence and intergranular or additional cleavage failure mechanism have been found on the fractured surface and the crack tip was under tensile loading. The plastic zone size in this final region was reported to be very much bigger than the grain diameter.

Many researchers have reported that fatigue failure in the Paris Region is generally by transgranular ductile striation mechanism (DSM).[12,17,18] The crack path is generally taken to be across the grains (or transcrystalline), although they may also propagate along the grain boundaries or intergranular depending on the material properties, loading and environmental conditions.[19] In this linear crack growth region, the crack tip is under tensile loading and the plastic zone size is reported to be greater than a grain diameter. The crack closure is low and mechanism of growth is by striation—alternating or simultaneous shear on two slip systems.[18] The conclusion[3,5,6,20] that microstructure has little or no influence on the FCG rate (FCGR) of metallic materials is often based on the frequent observation of DSM in the Paris Region in fractographs. One thing that must be noted is that most of the fatigue theories existing today—including that of crack extension,[18] crack path[17] and crack closure[21,22]—were propounded from experiments performed on non-ferrous materials. For example, two other phenomena that are associated with crack retardation across metallic materials in the literature are crack closure and interlocking. It is pertinent to note that crack closure effect may be more important for non-ferrous ductile metals. It is a common knowledge that the concept of crack closure and the use of effective stress intensity factor range (SIFR) was proposed by Elber.[21,22] This theory is based on the fact that plastically deformed surface wake is left behind as the crack propagates. He argued that there is a premature contact of the crack faces during unloading from tension in a fatigue test. This effect reduces the effective stress at the crack tip. Elber proposed the use of effective SIFR instead of the conventional SIFR in plotting fatigue curve. The mechanisms such as the plasticity-induced and the roughness-induced crack closure can cause retardation of the FCGR. However, it is pertinent to note that Elber's theory is based on his study of 2024-T3 aerospace aluminium alloy of a moderate ductility. The validity of this theory to steel will vary because (a) steel can have high ductility in annealed or fine-grained condition to 'near-brittle' ductility in martensitic or very low temperature condition and (b) the thickness effect in steel material. As sample thickness of steel is increased, the plain stress region at the outer surface tends to be eliminated, leaving only plain strain condition where plastic zone becomes little or almost negligible. Hence, the concept of crack closure may not be rigorously applied to steel at all conditions, coupled with the fatigue test condition under plain strain condition, that is, with little or negligible plastic zone at the crack tip. In other words, when the plastic zone is little, the effect of crack closure can then be ignored, or its consequences will be insignificant.

None of these studies in practical terms showed vividly how the crack propagated through the phases in the microstructure of the materials studied. There are many variables, for example, alloying elements and their concentrations, forming process and the mode of deformation, and heat treatment—involving temperature range, heating time and cooling time—which can be combined in so many ways to obtain varieties of steel properties (e.g., ranging from high ductility to almost completely brittle steel). The primary goal of this paper, therefore, is to present some observed microstructural influence on the FCG phenomenon in the Paris Region of ferrite–pearlite (α–P) steels produced by normalized rolled (NR) and thermomechanical control process (TMCP) in air and seawater (SW).

2 | METALLURGY AND CHARACTERIZATION OF PHASE CONSTITUENTS OF EXPERIMENTAL STEELS

The increasing demand for economic steels with higher toughness, better weldability and less expensive alloying elements has resulted to modern TMCP steels. These materials are increasingly being used in the design of offshore support structures. Some of the advanced marine steels and conventional steels are shown in Table 1. The TMCP steel grades have been manufactured specifically for offshore pipelines, platforms, pressure vessels and modern wind turbine installations.[28–30] Currently, they are replacing the more traditional ones in Table 1. The BS4360 Grade 50D is equivalent to S355J2 + N hot rolled normalized steel.

TABLE 1 Advanced marine steels and conventional steels

Offshore structural steel plates		
Advanced S355 steel subgrades for marine applications[23]		Conventional S355 structural steel grades[24–27]
European	Typical offshore application	European
EN10225		EN10025 part 2: 2004
S355G7 + N	Primary structure	S355
S355G7 + M	Primary structure	S355JR
S355G8 + N	Critical joints	S355JO
S355G8 + M	Critical joints	S355J2
S355G9 + N	Primary structure	S355J2 + N
S355G9 + M	Primary structure	S355K2
S355G10 + N	Critical joints	S355K2 + N
S355G10 + M	Critical joints	S355NL

Figure 1A is common Fe-C phase diagram showing important regions in the heat treatment of marine steels. γ denotes austenite, α ferrite and *P* pearlite. The lines in Figure 1A are straight; in fact, in the case above, they are drawn arbitrarily. In reality, the shape and position of the lines, straight or curved, depend on the steel chemistry, cooling rate and rolling or deformation variables. The nature of α–*P* microstructure due to heat treatment can be explained by the type of heat treatment process—commonly referred to as as-rolled (AR), normalized (N), NR, quenched and tempered (Q&T) and TMCP. The common phases in these steels are ferrite (α) and pearlite (α + Fe_3C). Figure 1B–F are schematic of heat treatment of modern steel. The heat treatments of interest in this study are AR, N, NR and TMCP. AR is obtained by austenitizing above Ac_3,[33] holding for specified time and then deforming at roughing and finishing mills within the austenite range and cooling naturally to room temperature as shown in Figure 1B. The N steel is commonly obtained when the AR is reheated to about 900°C or very little above Ac_3, held for a desired period and allowed to cool naturally back to room temperature as shown in Figure 1C.

When the finishing rolling operation is done at a temperature above about 900°C before cooling naturally to room temperature, an NR steel is obtained. The N and NR steels have practically the same properties and so are designated 'N'. The strength or other properties of the steel can be increased by addition of small amount of alloying elements and then quenched or accelerated cooled and tempered as shown in Figure 1D. The tempering is then done below Ac_1. TMCP is a microstructural control technique combining controlled rolling and accelerated cooling to obtain exceptional strength–toughness combinations in low-alloy steels by grain refinement.[32,34–36] The property obtained may not be different from those obtained after normalization.[31,32] The TMCP route is illustrated in Figure 1E,F.[31] Traditional marine steels shown in Table 1 are produced by AR, N or NR. The TMCP steels production route is proprietary, and so, processing conditions and number of

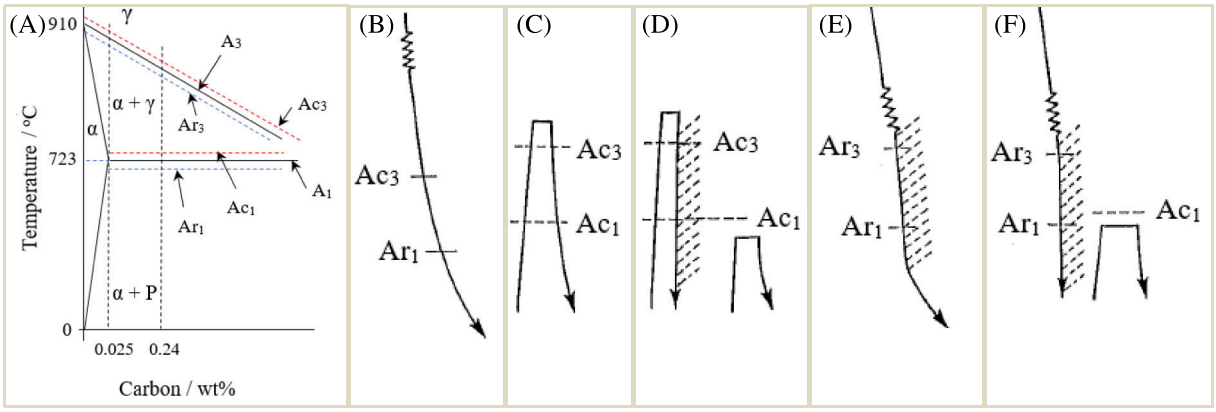

FIGURE 1 Heat treatments of modern steel. (A) A schematic phase diagram of carbon composition range and phases expected in the microstructure of marine steel; (B, C) rolling and normalization; (D) thermomechanical control process route involving reheating, accelerated cooling and self-temper or tempering at temperature below Ac_1; (E) rolling and accelerated cooling; and (F) rolling, direct quenching and tempering at temperature below Ac_1.[31,32] A_1 is an equilibrium lower transformation temperature (eutectoid reaction occurs at A_1, which is 723°C in the binary diagram). Ar_1 temperature depicts the lower transformation temperature upon cooling. Ac_1 temperature depicts the start point of the transformation between the α-ferrite and the austenite γ upon heating. A_3 is an equilibrium upper transformation temperature where alpha iron (α-Fe) transforms to gamma iron (γ-Fe) and it is 910°C for pure iron and it is lowered with addition of carbon. Ar_3 is the temperature at which austenite γ starts transforming to ferrite α during cooling. Ac_3 temperature depicts the upper transformation temperatures upon heating [Colour figure can be viewed at wileyonlinelibrary.com]

deformations are slightly different, producing what may appear as variation in the α and P sizes and morphologies.

Ideally, most common marine steels have microstructures consisting of very small volume fraction of P in α matrix. It may be called α–P steels where volume fraction of P phase is significant. The common α morphologies are grain boundary allotriomorphic α, idiomorphic α, Widmanstätten α, and intragranular α or acicular α.[37] The α morphologies commonly encountered in marine steels are the allotriomorphic and idiomorphic α. In this study, they will collectively be referred to as α. The microstructure shown in Figure 2A is air cooled of medium carbon steel, and the relatively rapid method of cooling limited the α grain growth. The α then appears to form layers, which followed the austenite grain boundary contours. The prior austenite grain boundaries are completely covered by the α allotriomorphs and the residual austenite has transformed into P upon reaching the temperature, 723°C, of eutectoid reaction. The α phase is soft and ductile, whereas the P is hard and brittle. P grows in colonies and each colony consists of a thin lamellar, alternating mixture of α (iron) and cementite, θ (iron carbide, Fe_3C). Figure 2B shows a situation where the Fe-0.4C steel is slowly cooled to room temperature, producing equiaxed grains. Several distinct P colonies can be seen (dark etching). As the volume fraction of P increases, the bulk strength increases and ductility decreases. If the carbon content of the steel is decreased, the volume fraction of P in the microstructure will decrease, whereas that of α increases as can be seen in Figure 2C. The morphology or shape of the α–P phases therefore depends on the processing route discussed above and chemical composition. These two phases are of major interest in this study and other phase that might be present for the purposes of clarity is neglected.

3 | EXPERIMENTAL MATERIALS AND TEST CONDITIONS

The steels for this study are S355J2 + N (J2N), S355G10 + M (G10) and S355G8 + M (G8) with compositions as given in Table 2. The composition of J2N was extracted from Steimbreger.[40] They are marine steels having low carbon contents with the microstructures consisting of small volume fraction of P in α matrix.[39] Figure 3 shows the phase morphologies of the J2N microstructure.

In Figure 3A, the optical micrograph shows that the microstructure is composed of P (dark etching) and the rest α (light etching). Microstructural examination of J2N shows that 80% of the microstructure is allotriomorphic α and others P, with traces of acicular or Widmanstätten α.[41] The P colonies in the J2N steel are large, blocky and dense. This is a consequence of its chemical composition, heat treatment and deformation or manufacturing method. Figure 3B is the scanning electron microscopy (SEM) micrograph of the microstructure. The blocky P and the proeutectoid α are noted accordingly. The proeutectoid α is the α phase that formed before the formation of P at the eutectoid temperature (723°C). Figure 3C is the part denoted with a yellow box in Figure 3B and the micrograph shows differently oriented P colonies as demarcated by the yellow lines. Figure 3D shows what would have been the image of the part in the yellow box in Figure 3C on a typical transmission electron microscopy (TEM) micrograph. The structure that appears as parallel rods in that colony is the cementite (θ). Figure 3D is extracted from Bhadeshia.[37] Figure 4 shows the microstructures of G10 and G8. These microstructures are found to be similar, but it is evident that they are distinct from that of J2N in Figure 3. Figure 4A is the optical image of G10, whereas Figure 4B is the SEM image. Similarly, Figure 4C is the optical image of

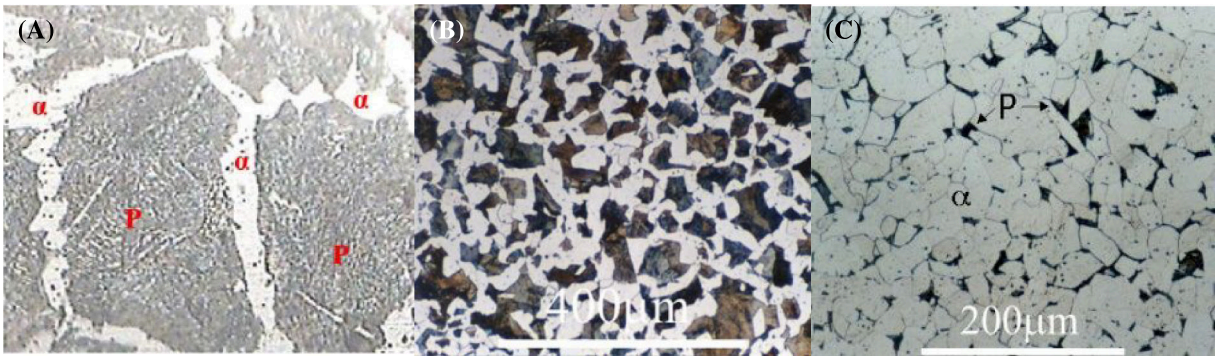

FIGURE 2 Ferrite and pearlite morphologies: (A) ferrite in Fe-0.46 steel that forms layer tracing the austenite grain boundary contours,[38] (B) equiaxed ferrite in a Fe-0.4C steel,[37] and (C) ferrite in low-carbon steel[37] (α = ferrite, P = pearlite). The white etching is ferrite, whereas the dark etching is pearlite [Colour figure can be viewed at wileyonlinelibrary.com]

TABLE 2 Chemical compositions and mechanical properties of test materials (see Igwemezie et al.[39])

Steel grade	Notation	C	Mn	Ni	Si	Cu	Cr	Mo	E%	YS (MPa)	UTS (MPa)
S355G10 + M (TMCP)	G10	0.06	1.57	0.33	0.27	0.24	0.03	0.01	38	435	545
S355G8 + M (TMCP)	G8	0.05	1.52	0.32	0.27	0.24	0.03	0.01	35	447	549
S355J2 + N (NR)	J2N	0.17	1.54	0.04	0.04	0.08	0.02	-	20	385	531

Abbreviations: NR, normalized rolled; TMCP, thermomechanical control process.

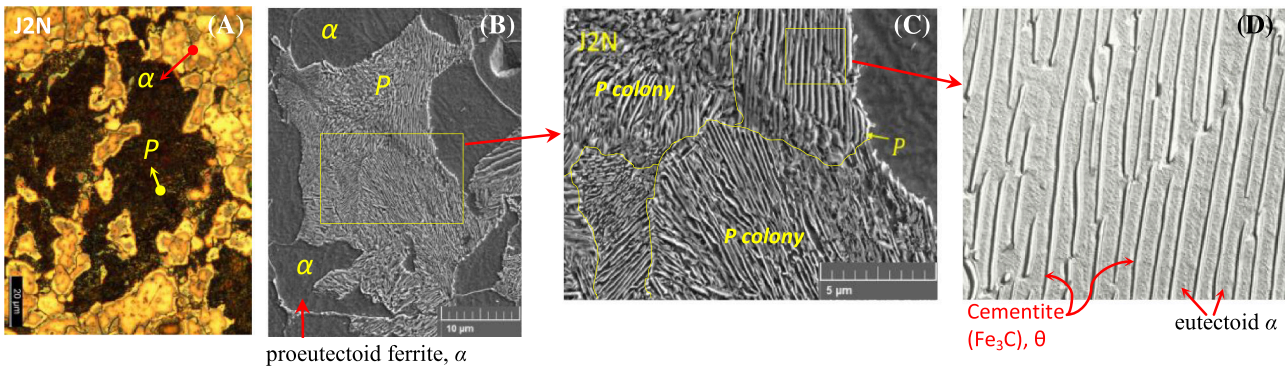

FIGURE 3 Photomicrographs of α–P steels. Normalized rolled—S355J2 + N [Colour figure can be viewed at wileyonlinelibrary.com]

G8, whereas Figure 4D is the SEM image. It is evident that the SEM image shows more details of the microconstituents. In both microstructures, the P nodules are very small compared with that of J2N and the volume fraction of the P is also less than that of J2N.

Figure 5 shows the morphologies of the phases present in J2N in the rolling direction. The ferrite phase tends to have three forms, and are referred here as high relief (HR), low relief (LR) and ribbon like structure (HA) as shown in Figure 5A. Note that the low and high relief α phase variants could not be distinguished under optical micrographs (see Figure 3A). These features are important in analysing the work presented in this paper. For the purposes of description, let α_{HR} denote α with high relief and α_{LR} is low relief, whereas the ferrite ribbon is denoted α_{HA}. The yellow arrow shows the P, the blue arrow indicates the α_{HA}, the red arrow is the α_{HR} and the black arrow is the α_{LR}. To the extent of information available to the authors, the α phase morphologies observed in Figure 5A are novel and have not been described elsewhere. Figure 5B–D shows the energy-dispersive x-ray (EDX) analyses of the elemental composition of the phases present in the J2N at locations 1 to 31, and the results are shown in Table 3. The relative abundance of the alloying elements in the phases is in wt %. Note that the EDX analysis, as presented, simply shows the relative abundance of the alloying elements within a micrometre or nanometre area in the phase and has no direct relationship with the steel overall composition shown in Table 2.

In Figure 5B–D, locations 1, 3, 4, 16, 21, 30 and so on are areas of analyses on the α_{HR}, whereas 2, 5, 17, 25,

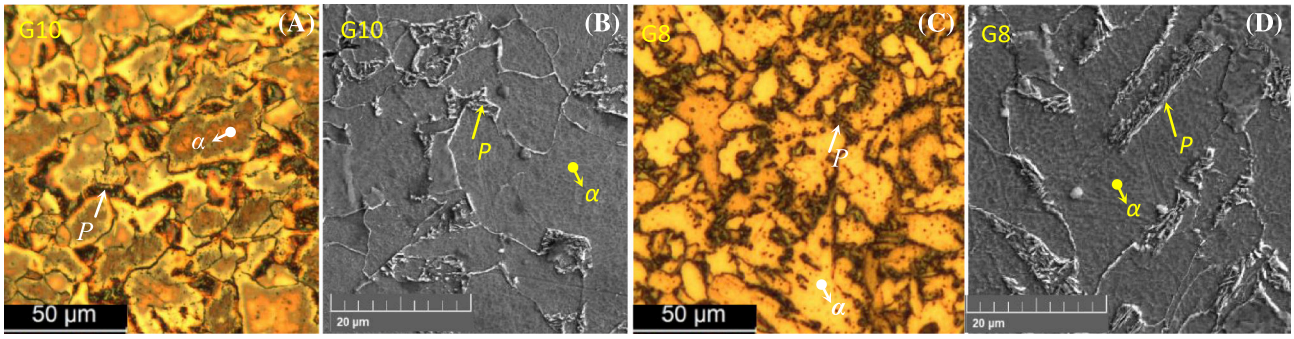

FIGURE 4 Optical (A, C) and scanning electron microscopy (B, D) micrographs of ferrite, α, and pearlite, P, phases in the thermomechanical control process steels [Colour figure can be viewed at wileyonlinelibrary.com]

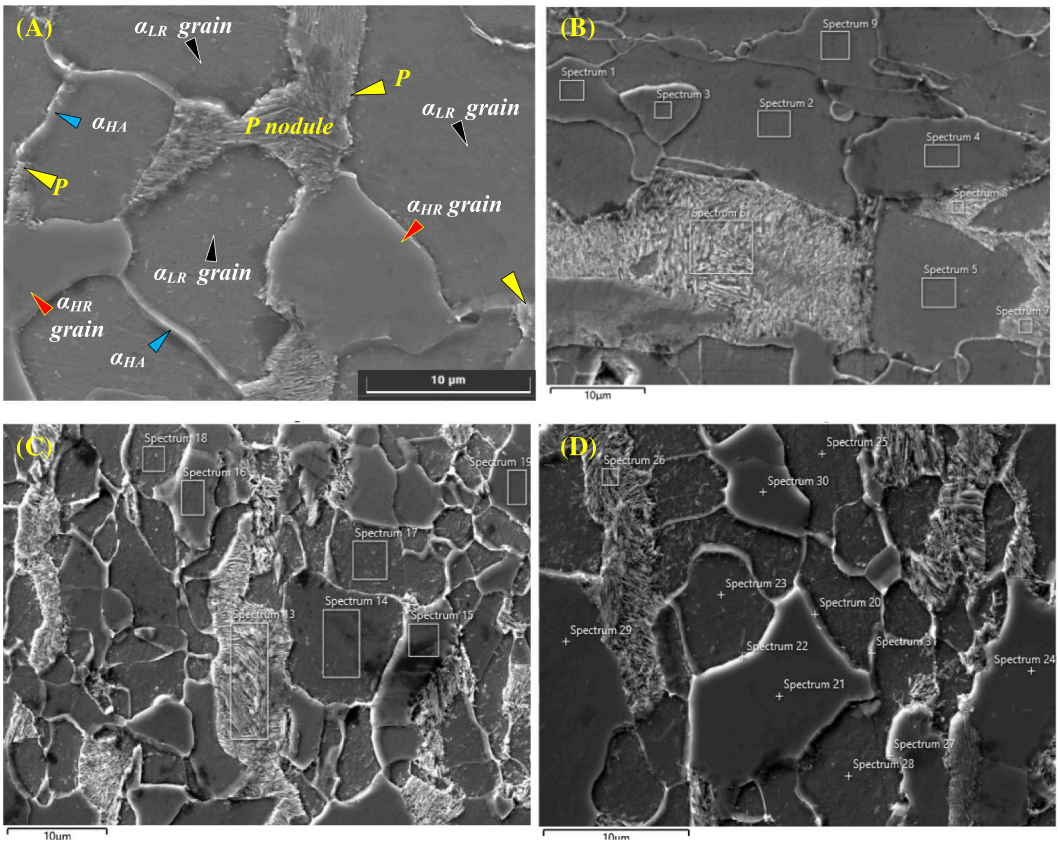

FIGURE 5 Energy-dispersive x-ray analysis of phase composition in S355J2 + N steel in the rolling direction [Colour figure can be viewed at wileyonlinelibrary.com]

28 and so on are areas on the α_{LR}. The light etching is the *P*, for example, locations 6, 7, 8, 13, 26 and so on. In Table 3, simple observation of the EDX results shows that the alloying compositions of α_{LR} and α_{HR} are almost the same. But for the α_{HA}, all other alloy compositions are generally the same with that of α_{LR} and α_{HR} except that the amount of C, Si, Al and O are higher. The Fe content of α_{HA} and *P* are close, but lower than those of α_{LR} and α_{HR}. This tends to suggest that α_{HA} is a ferrite phase with the highest concentration of alloying solutes. The *P* is found to have generally the same composition with the α_{HA}, but with higher oxygen content. An important note here is that the concentration of these solutes may weaken this phase, making it an easy path for FCG. Commonly observed phase morphologies of J2N, G8 and G10 are shown in Figure 6. Figures 6A and 6B are that of J2N obtained in the through thickness direction. The same basic microstructural features found in Figure 5A were also observed in Figure 6A,B. Figure 6C–I presents microstructural features in the TMCP steels that are basically the same as that found in the J2N steel. For the TMCP, the *P* formed mainly between boundaries of the ferrite grains and with width that is relatively small. In the J2N steel, *P* forms as dense and blocky phase in the α matrix. The formation of these microstructural phase morphologies created different local microstructural properties. The presence of a hard phase (*P*) in a soft matrix (α) is expected to influence local FCG behaviour in steel.[42] The crack paths in these microstructures are also expected to vary. Compact tension C(T) specimens

TABLE 3 Energy-dispersive x-ray analysis compositional average results of α and *P* phases in Figure 5

Spect. label	C	Mn	Ni	Si	Cu	Cr	Mo	Al	Co	P	S	O	Fe
α_{LR} average	5.50	1.41	0.09	0.37	0.02	0.02	0.01	0.12	0.41	0.02	0.01	0.10	91.79
α_{HR} average	5.59	1.36	0.08	0.37	0.02	0.02	0.01	0.12	0.40	0.02	0.01	0.07	91.79
α_{HA} average	9.86	1.41	0.09	0.46	0.04	0.02	0.01	0.17	0.39	0.03	0.01	0.45	88.12
P average	9.33	1.50	0.08	0.40	0.06	0.02	0.01	0.11	0.38	0.02	0.02	1.38	86.59

Abbreviations: HA, α ribbon; HR, high-relief α; LR, low-relief α.

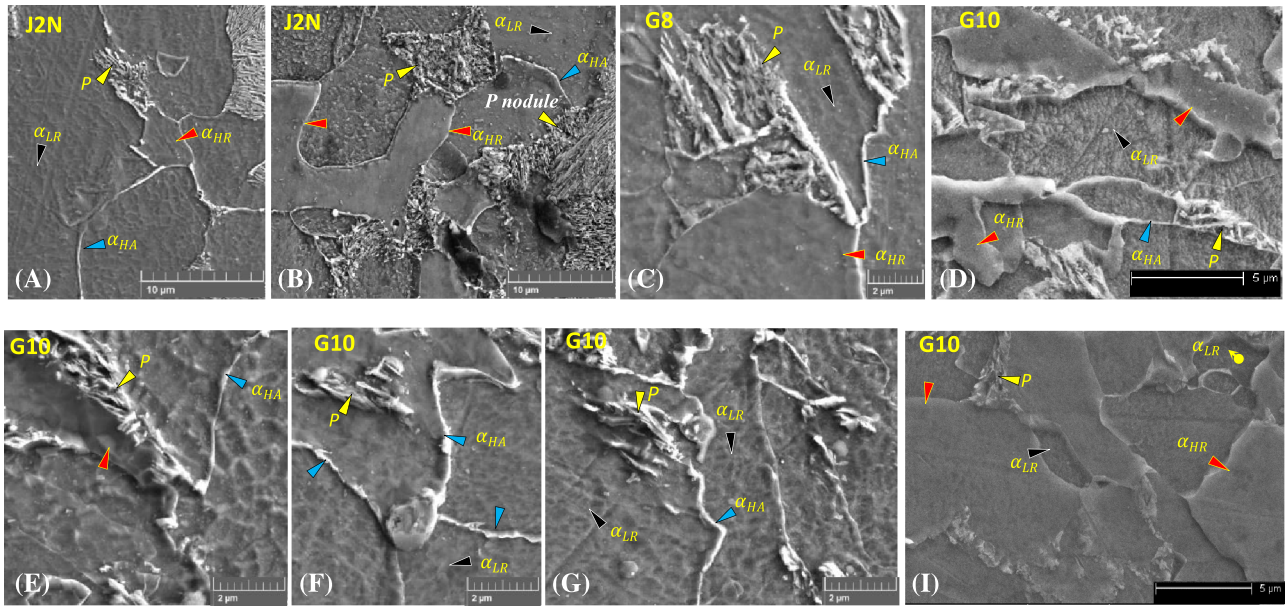

FIGURE 6 Phase morphologies of J2N, G8 and G10 S355 steel subgrades showing α and P phases [Colour figure can be viewed at wileyonlinelibrary.com]

extracted from the midthickness of a 90 mm thick plates were used in this study. The test set-up, loading conditions, crack growth monitoring, estimation and FCGR calculations are presented in detail in other studies.[23,39,43]

4 | FCGRS IN NR AND TMCP S355 STEELS IN AIR

Steel microstructure influences fatigue crack propagation primarily by changing the mode of crack propagation. The mode can change from ductile striation to cleavage mode and the combination of the two modes increases crack propagation rates. There are many studies that claimed that microstructure has negligible effect at intermediate FCGRs (Paris Region).[3,5,6,13–16,20] Some other study concluded that grain size affected subcritical crack growth to the extent to which it affected fracture toughness, K_{Ic} and the onset of rapid fracture and that grain size did not affect the FCG threshold, $\Delta K_{th.}$[4] Zerbst[6] in his recent publication reported that '... Perhaps the most astonishing observation is that the curve, in the Paris Region, is only slightly influenced by the microstructure of the material within whole material classes such as steels or aluminium alloys.' In fact, it is commonly reported that microstructure has little or no influence in the Paris Region of the *da/dN* sigmoidal curve in air. Part of the presentation in this paper is to show what appears to be an influence of the FCGR by microstructural phase morphologies in the Paris Region of the *da/dN* versus ΔK curve.

In the recent studies, the authors evaluated the resistance of the NR and TMCP steels given in Table 2 to FCG. The experimental methods have been discussed in full elsewhere.[23,39,43] The results of that study, for FCGR tests in air, are shown in Figure 7. Shown also are the typical microstructures of the J2N and TMCP (G10 and G8) steels examined. In Figure 7, it appears that there is a demarcation between the FCGR of NR and TMCP in the Paris Region. The arbitrary line drawn as shown appears to be the separation line. The FCGR in G8 and G10 steels are essentially the same and significantly lower than that of the J2N steels under the same experimental conditions. Generally, the FCGR increased with increase in load level from 10 to 12 kN in J2N and also from 9 to 10 kN in TMCP. This is the expected trend in air, where increase in the fatigue load level increases the FCGR. We can also observe that the FCGRs in J2N for 10 kN under 2 and 5 Hz are essentially the same. This tends to confirm that frequency has no effect on the FCGR of steel in air under the same loading conditions. To validate this finding, a comparative study of FCGR in NR and TMCP was carried out. The steel grade, chemical composition in wt % (approximated to two decimal places) and mechanical properties of the steels studied and compared with the data in this study are included in Table 4. The composition range for the steels in Table 4 is shown in Table 5. It is pertinent to note that BS4360 Grade 50D, Q345, RD480 and EH36 are equivalent to S355J2 + N hot rolled normalized steel. Q345 is common structural steel in China and used in the nuclear industry and

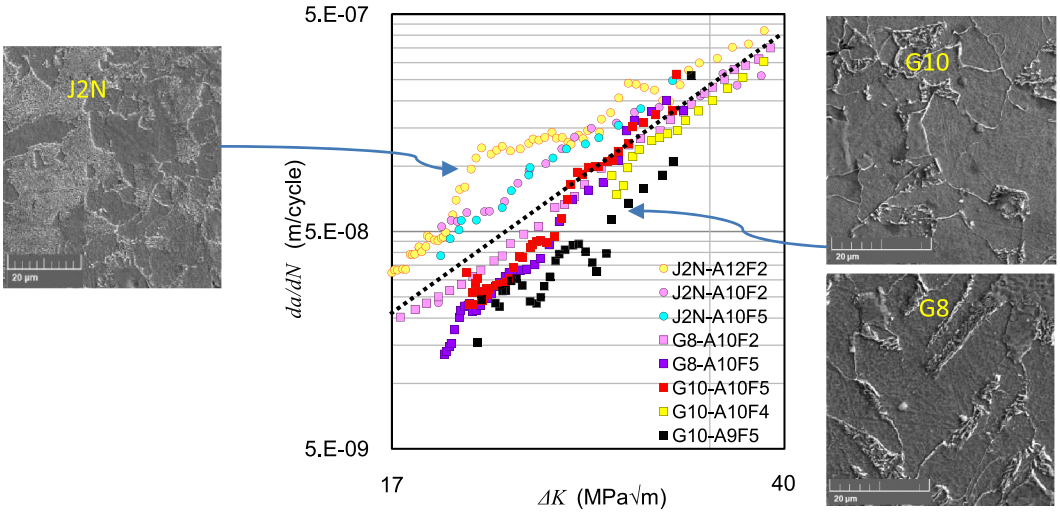

FIGURE 7 Plot of fatigue crack growth rate in air for normalized rolled (J2N) and thermomechanical control process steel subgrades (G8 and G10) [Colour figure can be viewed at wileyonlinelibrary.com]

petrochemical plants. Laurito[53] studied FCGR in intercritical isothermally quenched grain modified steel designated as RD480. Though the chemical composition is comparable with other steels, the properties of the microstructure generated may differ significantly due to this heat treatment. Two microstructures of the same ABS grade EH36 steel produced by NR and TMCP are presented. This steel is often used in shipbuilding. Comparing these two microstructures of the same alloy will clearly support this study. Table 6 lists all the studies and test conditions considered. All the steels are designed to be used in both onshore and offshore structures. They are fundamentally the same. The only difference perhaps is that the steels were produced under different proprietary methods by different steel plants. All the tests were done under constant-amplitude sinewave, except Cheng[54] who performed his test under random waveform. The general range for temperature of the studies is about 27°C to 0°C. From the conclusions in the literatures,[47,50,60–64] stress ratio (R) in the range 0.1–0.85, frequency in the range 0.005–50 Hz and waveforms appear to have little or no effect on the *FCGR* in the α–P steels in air. Thus, the inferences here are within these limits.

The marine steels have microstructures consisting essentially of small volume fraction of P in α matrix. The morphology of the phases varied from banded to unbanded depending on the production process and sample thickness. The general microstructures of the steels in Table 4 are shown in Figure 8. The grade of steel and the reference sources are also given. Figures 8A to 8D are microstructures of NR steels. The black etching is a banded P forming in the rolling direction and the light etching is the α. Figures 8E and 8f are microstructures of the same NR steels, but taken from directions that are unbanded.[41] Figure 8G is TMCP microstructure of the EH36 steel studied by Tsay.[56] The microstructure of TMCP steels is greatly refined as compared with those of conventional or NR steels, resulting in a significant improvement in strength and toughness. Hardness was measured to be around 168$HV_{0.1}$ with equiaxed grains of average size of 15 µm, measured in the through thickness direction. Figure 9 presents the plots of the *FCGR* studies on the *NR* and *TMCP* steels listed in Table 6, including the results of the present study (*PS*) from Figure 7. For the test IDs in the *PS*, each sample is denoted with material type (e.g., J2N, G8 and G10), followed by the environmental air (A), the maximum load applied, P_{max}, on the sample (e.g., 10 kN), and the applied f (e.g., F of 0.2, 0.3 and 0.5 Hz). The NR data points are denoted with circles in Figure 9. The J2N data points in the PS are coloured yellow, and the NR data points extracted from the literatures are green or black. The TMCP data points are denoted with squares. The same trend observed in Figure 7 is also seen in Figure 9. It can be observed that in the Paris Region taken in the interval $20 \leq \Delta K \leq 35$, the FCGR for the two microstructures separated into two domains, but with diffused interboundaries. The dashed line is drawn arbitrarily to show possible demarcating line. Occupying the upper half are the fatigue data points of NR steels and the lower half are the FCGR data points for the TMCP. In other words, the FCGRs in NR are generally higher than that of TMCP in air.

One interesting note here is that even though the steels have similar microconstituents, the FCGRs are significantly apart, especially at low SIFR. Often, many

TABLE 4 Chemical compositions of the ferritic steels for comparative study

Study	Steel grade	C	Mn	Ni	Si	Cu	Cr	Mo	E%	YS (Mpa)	UTS (Mpa)
Scott[44]	BS4360-50D (NR)	0.18	1.38	-	0.37	-	-	-	32	370	538
Appleton[45]	BS4360-50D (NR)	0.13	1.22	-	0.32	-	-	-	32	368	508
Thorpe[46]	BS4360-50D (NR)	0.17	1.35	0.07	0.35	0.17	0.09	0.01	32	370	538
Musuva[47]	BS4360-50D (NR)	0.18	1.40	0.10	0.36	0.16	0.11	0.02	30	386	560
Thompson[48]	BS4360-50D (NR)	0.15	1.38	0.10	0.41	0.02	0.11	0.01	30	386	536
Correia[49]	P355NL1 (NR)	0.13	1.38	0.12	0.35	0.14	0.03	0.00	-	418	568
Jesus[50]	EN 10025 S355 (NR)	0.10	0.64	0.10	0.15	0.38	0.08	0.01	22	419	766
Adedipe et al.[51]	S355J2 + N (NR)	0.22	1.60	0.50	0.55	0.55	0.03	0.10	20	345	-
Xiong[52]	Q345 (NR)	0.15	1.54	-	0.34	-	-	-	26	370	585
Laurito[53]	RD480 (IGM)	0.09	1.17	0.01	0.05	0.01	0.02	0.01	32	459	541
Cheng[54]	EH36 (NR)	0.12	1.39	0.03	0.38	0.05	0.05	0.01	21	350	-
Callister[55]	K-50 (TMCP)	0.05	1.13	0.29	0.23	0.24	0.02	0.20	-	470	-
Tsay[56]	EH36 (TMCP)	0.13	1.32	0.03	0.31	-	0.03	-	21	420	-
Chapetti[57]	UFG—Steel (TMCP)	0.15	1.80	-	0.20	-	-	-	14	696	1183
PS (T)	S355G10 + M (TMCP)	0.06	1.57	0.33	0.27	0.24	0.03	0.01	38	435	545
PS and Ali[58,59]	S355G8 + M (TMCP)	0.05	1.52	0.32	0.27	0.24	0.03	0.01	35	447	549

Note. BS4360 Grade 50D, Q345, RD480 and EH36 are equivalent to S355J2 + N hot rolled normalized steel. Average wt% of other minor elements for all the steels: 0.01 Ti, 0.02 V, 0.01 N, 0.02 S, 0.02 P, 0.03 Al, 0.04 NB.
Abbreviations: IGM, isothermally grain modified; NR, normalized rolled; PS, present study; TMCP, thermomechanical control process; UFGS, ultrafine-grained steel.

TABLE 5 Composition ranges of ferritic steels in this study

C	0.05–0.22
Mn	0.60–1.80
Ni	0.01–0.50
Si	0.05–0.94
Cu	0.01–0.55
Cr	0.02–1.23
Mo	0.01–0.52

researchers associate this variation in the Paris Region with material variability or crack closure (*R* factor), but we could see that the margin of separation is very much significant—up to a factor of about 4 from the two extremes. An important observation also is that the FCGRs of the two microstructural variants (NR and TMCP) of the EH36 steel studied by Cheng[54] (NR) and Tsay[56] (TMCP) under similar experimental conditions are different. The FCGR data of the EH36 (NR) denoted with black circle are partitioned into the NR domain, whereas that of EH36 (*TMCP*) separated into the TMCP domain as shown by the black square. Note that within this region, the effect of crack closure is insignificant or negligible. In general, this result tends to suggest that microstructure affected the *FCGR* in air.

4.1 | Microstructure and FCG path in air

Post-failure examination of the fatigued surfaces in air revealed features shown in Figure 10. The fractographs in Figure 10A,B were obtained from the NR steel (J2N), whereas that of Figure 10C,D were obtained by Adedipe[67] for the same steel grade. Figure 10E is the fractograph obtained in air for the TMCP steel and the part in a red box was magnified as shown in Figure 10F. The area in the red box in Figure 10G was also magnified to that shown in Figure 10H. From all the fractographs, it is very obvious that the failure in air had occurred by DSM with secondary crackings (SCs) as shown by the arrows. Few SCs in the normalized steel, J2N and more SCs in the TMCP were observed. The occurrence of the SC increased with increase in SIFR. Striations were seen even inside the secondary cracks as can be seen in Figure 10F,H. This shows that the groove was made by a moving crack front and not due to brittle cracking or cleavage. The DSM as seen in the fractograph is typical of the failure mechanism in the Paris Region for low-carbon steel. These fractographs do not give significant clue to the observed difference in the FCGR in Figure 7 and Figure 9. An altervative approach is to examine the crack path and the features influencing crack growth in the materials.

TABLE 6 Experimental conditions for the studied steels in Table 4

Study by	Steel grade	Wave form	Frequency (Hz)	*R*	%EL	YS (MPa)
Scott[44]	BS4360-50D	s	1–10	0–0.85	32	370
Appleton[45]	BS4360-50D	s	-	-	32	368
Thorpe[46]	BS4360-50D	s	1–10	0.5	32	370
Musuva[47]	BS4360-50D	s	30	0.08, 0.5, 0.7	30	386
Thompson[48]	BS4360-50D	s	0.5	0.1	30	386
Correia[49]	P355NL1 (NR)	-	-	0.0	-	418
Jesus[50]	S355	s	≤20	0.25, 0.5 and 0.75	22	419
Adedipe et al.[51]	S355J2 + N	s	2	0.1	20	345
Xiong[52]	Q345	s	0.5	0.1–0.5	26	370
Laurito[53]	RD480	s	10	0.1	32	459
Cheng[54]	ABS grade EH36	r	10	0.1 and 0.5	21	350
Callister[55]	Kontroll-50 (TMCP)	s	0.5	0.6	-	470
Tsay[56]	EH36 (TMCP)	s	5	0.1	21	420
PS (T)	S355G10 + M (TMCP)	s	4 and 5	0.1	38	435
PS and Ali[58,59]	S355G8 + M (TMCP)	s	2 and 5	0.1	35	447

Abbreviations: NR, normalized rolled; PS, present study; r, random; s, sine; TMCP, thermomechanical control process.

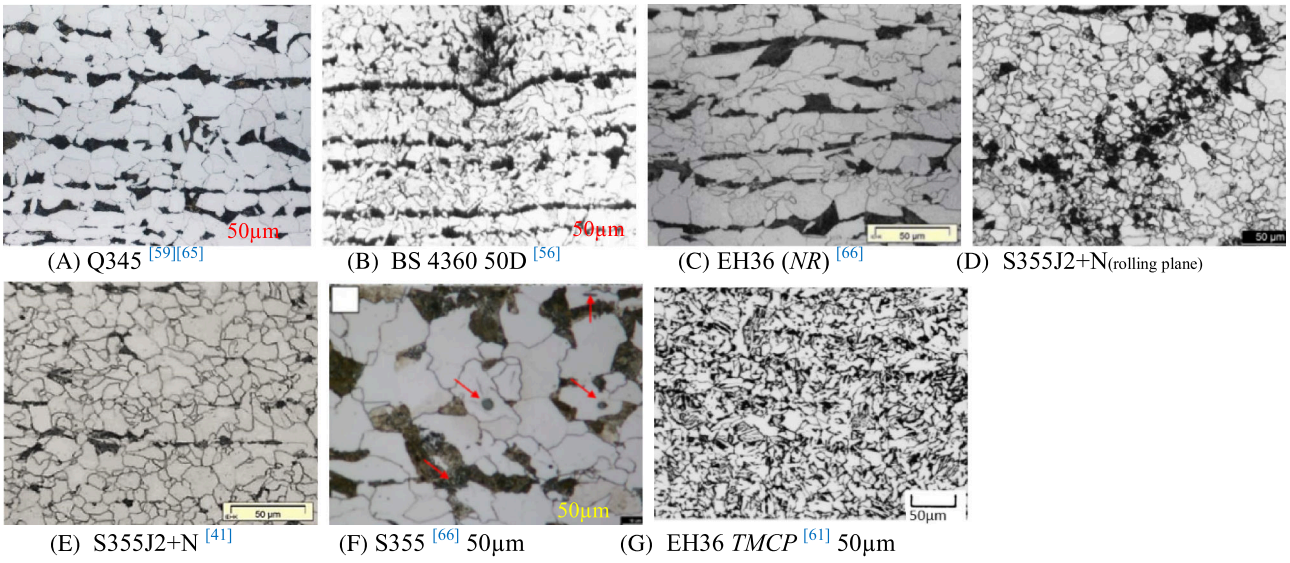

(A) Q345 [59][65] (B) BS 4360 50D [56] (C) EH36 (*NR*) [66] (D) S355J2+N(rolling plane)

(E) S355J2+N [41] (F) S355 [66] 50µm (G) EH36 *TMCP* [61] 50µm

FIGURE 8 Typical microstructures of low-alloy α–*P* steels. (A) Q345,[52,65] (B) BS 4360 50D,[48] (C) EH36 (NR),[66] (D) S355J2 + N (rolling plane), (E) S355J2 + N,[41] (F) S355[66] 50 µm, and (G) EH36 TMCP[56] 50 µm. NR, normalized rolled; TMCP, thermomechanical control process [Colour figure can be viewed at wileyonlinelibrary.com]

To understand the disparity in the FCGR between NR and the TMCP steels as presented in Figure 7 and Figure 9, a crack path metallography was carried out and the result is presented in Figure 11 for the TMCP steel, G8. Figure 11A shows the general crack paths seen in the TMCP steels in air for 10 kN, 5 Hz and stress ratio of 0.1, under sinewave. The yellow double line arrow in the figures shows the direction of the applied fatigue load. The long crack path was obtained for ΔK of about 18.52 to 34.25 MPa$\sqrt{m}$, that is, fully in the Paris Region. It is very clear that the crack path is non-planar and complex. The traces of the crack path are given in Figure 11B. The crack path has extensive high degree of large angle crack diversions, multiple bifurcations and crumb formations as noted clearly in Figure 11B.

The metal crumbs were formed in between branched and rejoined crack fronts. It can also be observed that several small metal crumbs were formed

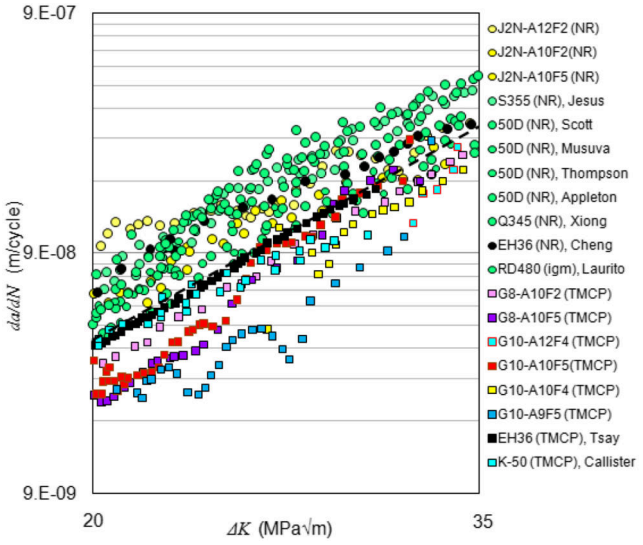

FIGURE 9 The fatigue crack growth rate in NR and TMCP in air in the Paris Region with demarcation line. NR, normalized rolled; TMCP, thermomechanical control process [Colour figure can be viewed at wileyonlinelibrary.com]

as the crack propagated in air and the occurrence increased with increase in ΔK. In other words, the tendency for crack branching and rejoining tends to increase with increase in the driving force for crack propagation. The length of the branched crack is considerably long, and the extent of bifurcation angle is substantially large. Figure 11C is the magnification of locations 1 to 8 marked with the yellow boxes. It was observed that the branched crack fronts generally followed the thin ribbon α_{HA} phase as shown in the magnified locations. This tends to suggest that α_{HA} is the path of least resistance. An important feature of the crack growth is that, generally, the tip of the propagating crack was always sharp as can be seen from the tip of the branched crack front as shown in the magnified micrographs in Figure 11C. The crack tip maintained its sharpness throughout the Paris Region in the range 18.52 to 34.25 MPa$\sqrt{}$m. The fact that α_{HA} could influence crack front diversion in the Paris Region is very important in the design of fatigue-resistant steel. The fractographs of fatigued surfaces as shown in Figure 10 can only show mechanism of the growth but cannot show these phenomena found in Figure 11 especially the formation of the metal crumbs, which has not been reported in any literature. Due to many branched and arrested cracks, it is expected that the fractography of the fractured surface for this sample will likely show many occurrences of SCs. This is evident in Figure 10E, G where many secondary cracks are present.

Figure 12A shows the crack path observed in NR steel in this study. Relative to the crack morphology in the TMCP (see Figure 11A), low-angle crack diversion and low-angle, short-length branching were seen. The red arrows show the low-angle crack diversion, the black arrows the low-angle crack branching and the white arrows show some metal bits or crumbs. Figure 12B is the schematic of the crack path showing clearly the enumerated features. This NR crack path is clearly different from that of the *TMCP* (Figure 11B), and it is a function of the microstructural features. In comparison with the crack growth path in J2N, the crack path in the TMCP is more complex with extensive high-angle crack diversion

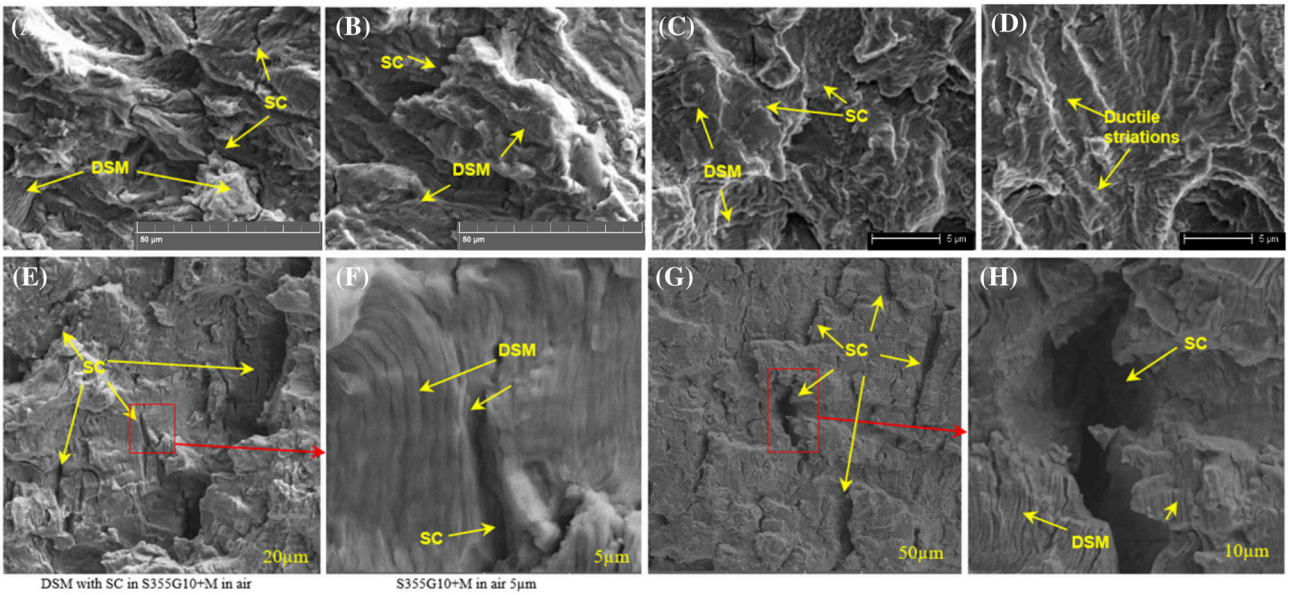

FIGURE 10 Fractographs of fatigued surfaces for (A–D) J2N and (E–H) G10 in air [ductile striation mechanism (DSM) with secondary crack (SC)] [Colour figure can be viewed at wileyonlinelibrary.com]

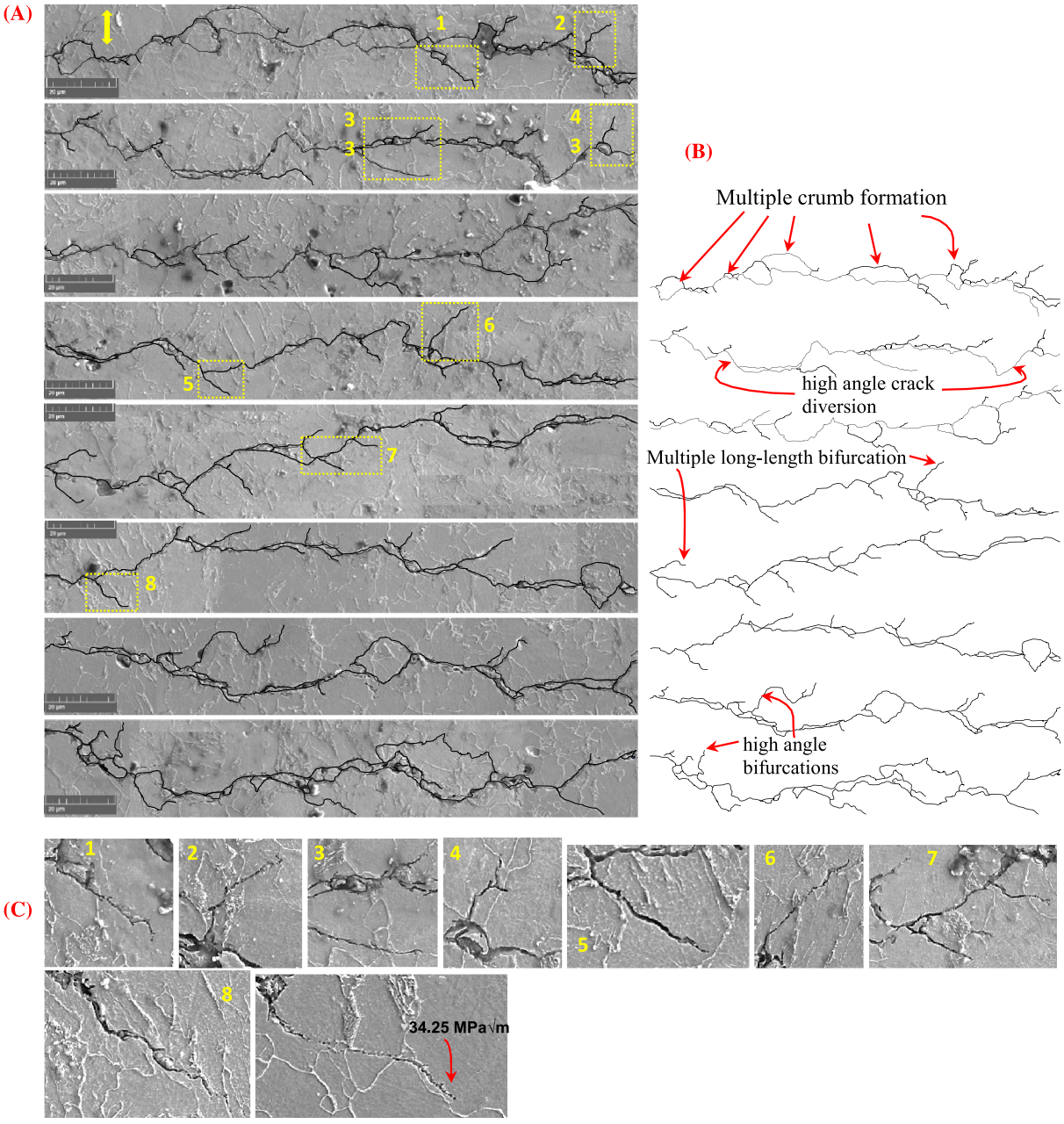

FIGURE 11 (A) Crack path in thermomechanical control process steels in air: G8, 10 kN, 5 Hz, sinewave, crack length between about 20.33 (18.52 MPa√m) to 30.09 mm (34.25 MPa√m). (B) Schematic of the crack path. (C) Magnification of the crack front (direction: from left to right) [Colour figure can be viewed at wileyonlinelibrary.com]

and crack branching. The lengths of the branched cracks are considerably longer than that of J2N. There was also severe formation of relatively large metal crumbs in air in TMCP than in J2N. Several small metal crumbs were also seen as the ΔK increased. The crack tip diversion, branching and creation of metal crumbs can reduce the effective stress at the local crack tips, resulting in retardation of the FCGR. Fundamentally, the degree of crack tip stress shielding will vary with the angle of crack tip diversion and the nature of metal crumbs created. The metal bit will be effective in retarding the crack growth if it reorients and causes mismatch or wedging action. The tendency to reorient may increase if the crumbs are smaller in rough-round shape rather than in plate-elongated form. These two natures of metal crumbs will be a function of the steel microstructure.

Figure 13 shows the FCGRs in two samples of the NR (the circle data) and three samples of the TMCP (the square data) steels. As noted, the tests were performed in air under similar test conditions at 10 kN and 2 Hz and 5 Hz for three materials—J2N, G8 and G10. Note that the microstructures of G8 and G10 are generally the

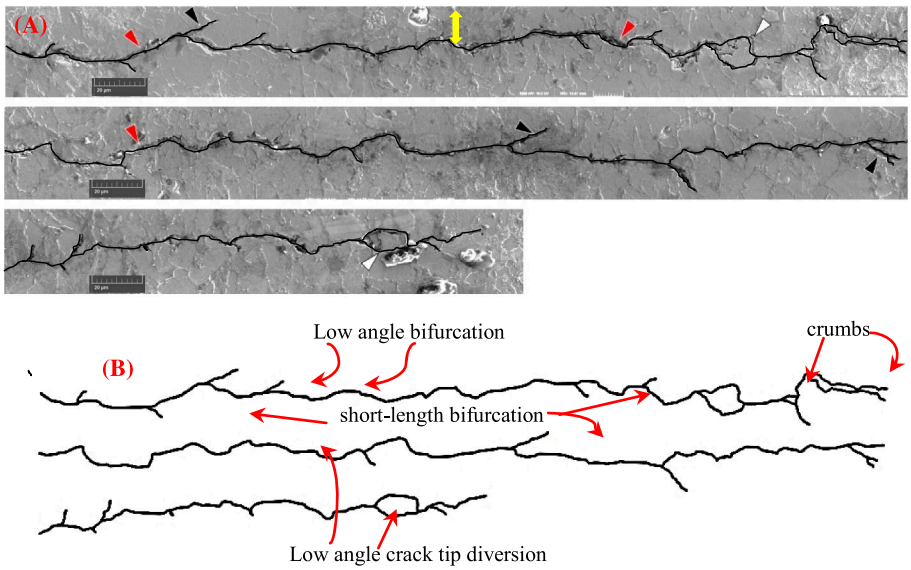

FIGURE 12 (A) Fatigue crack path in J2N steel in air (10 kN, 5 Hz) and (B) schematic of the crack path (direction: from left to right) [Colour figure can be viewed at wileyonlinelibrary.com]

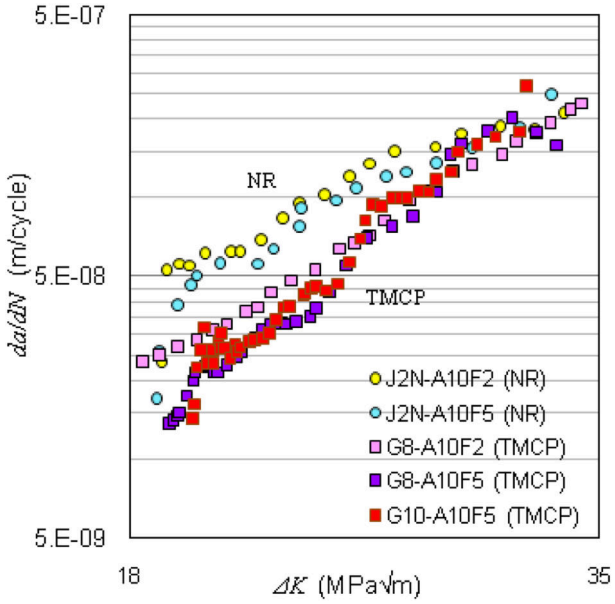

FIGURE 13 Fatigue crack growth curves in NR and TMCP steels. NR, normalized rolled; TMCP, thermomechanical control process [Colour figure can be viewed at wileyonlinelibrary.com]

same (see Figure 4). The FCGRs at 10 kN and 2 Hz (J2N-A10F2) and that of 10 kN and 5 Hz (J2N-A10F5) are generally the same, though that of J2N-A10F2 is slightly higher. This may be because the maximum fatigue loading, P_{max}, can be fully delivered during test at reduced frequency. Generally, these tests show that the effect of frequency on FCGR in air is negligible within the same steel subgrade. An important feature of the crack growth is that, generally, the tips of the propagating cracks in the TMCP steel are always sharp throughout the Paris Region (see Figure 11C). High-angle crack bifurcation and diversion are generally absent, and the formation of metal crumbs is few in the NR steel. This explains the reason for the higher FCGR in the NR as compared with the TMCP steel. This implies that the longer the branched arms, the more the diversions and branching angles and the more the crack growth is retarded due to redistribution and reduction of the driving force at the main crack tip. Where the three phenomena are few, one would expect a high FCGR.

4.2 | Assessment of FCGR path and mechanism in air

From the previous discussions, it is obvious that the material microstructure influenced the FCGR by crack path diversion, branching and formation of metal crumbs in between branched and rejoined crack fronts. High FCG retardation was obtained when large angle diversion, large angle branching and change in the orientation of metal crumbs occurred. Some of the distinct micrographs showing phases and morphologies influencing the FCGR are presented in Figure 14 for the NR steel and Figure 15 for the TMCP steel. The phases were obtained by scanning along the entire length of the fatigue crack from the initiation point to point of test stoppage.

Figure 14A–C shows instances of the propagation of the crack that initiated from the C(T) specimen notch of length 20.50 mm. In existing theory, a long crack is regarded as a fully developed crack with attendant plasticity-induced crack closure effect and of length usually greater than 0.5 mm,[20] the plastic zone is larger than one-fiftieth of the crack length ($r > 1/50a$) and the rate of crack propagation is described by the Paris law. At a length of 20.50 mm, the crack shown in Figure 14 is a very long

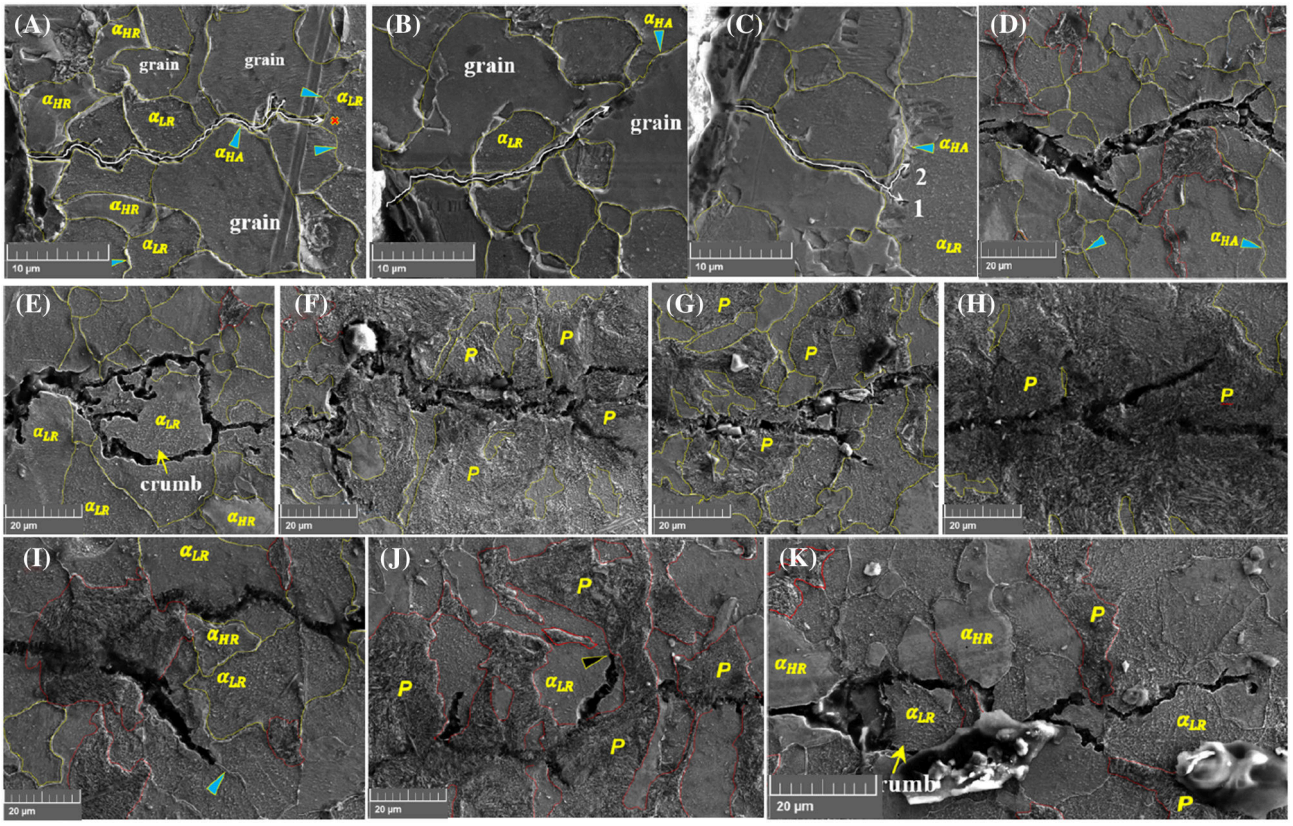

FIGURE 14 Effect of microstructure on fatigue crack growth rate in normalized rolled steel in air, for 10 kN and 5 Hz [Colour figure can be viewed at wileyonlinelibrary.com]

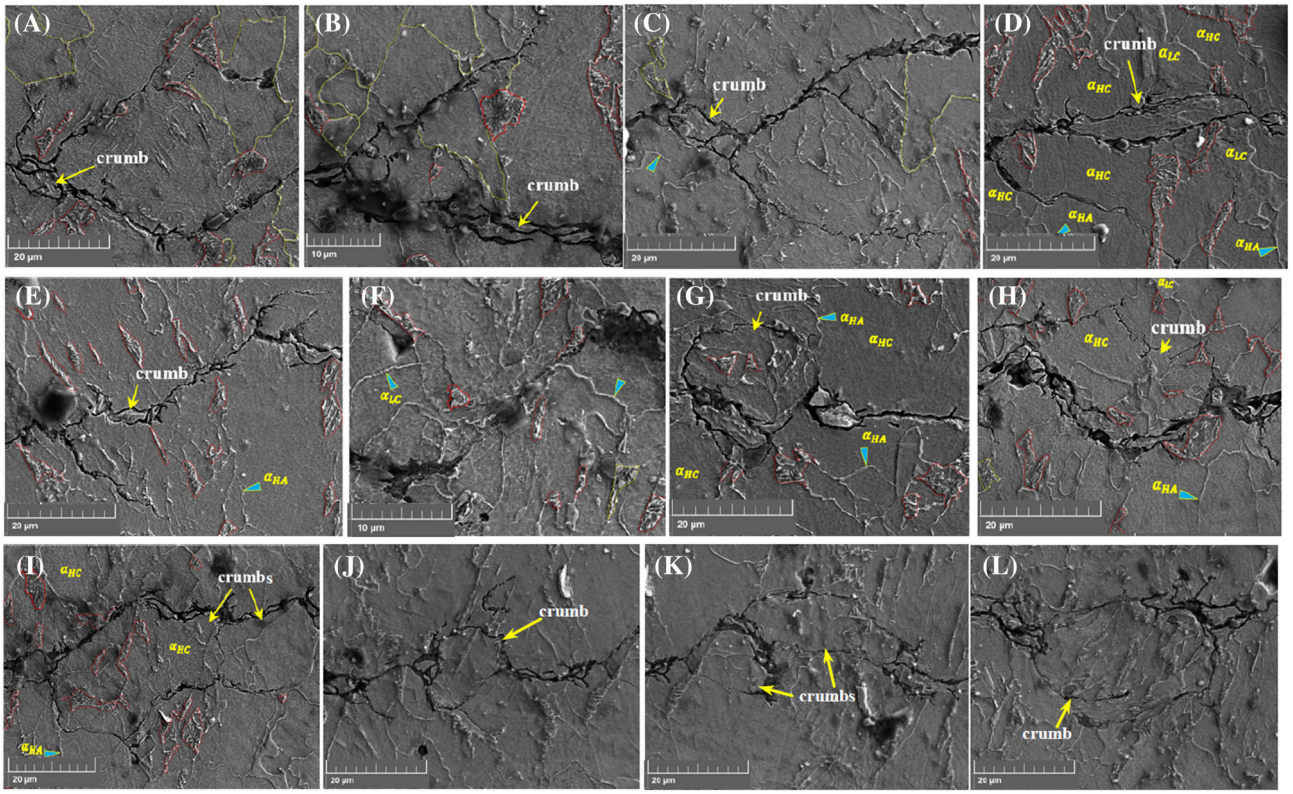

FIGURE 15 Fatigue crack growth in thermomechanical control process, G8, 10 kN and 5 Hz in air [Colour figure can be viewed at wileyonlinelibrary.com]

one. The dotted yellow line shows the boundaries of the grains. The encircled spaces by the yellow dotted lines are the ferrite grains, whereas the red dotted lines, where used, encircled the pearlite nodules. The white solid line shows the movement of the fatigue crack through the microstructural phases. The end dots in Figure 14A showed crack fronts that stopped growing, whereas the arrow indicates the mean active crack front. In Figure 14A–C, the crack appears to have initiated from and then propagated along what appears as the grain boundaries or 'intergranularly'. A closer observation shows that the crack propagated through the thin ribbon of the high alloy ferrite phase, α_{HA}, that surrounds the α_{LR} grain surfaces. This crack path as observed can be described as a *quasi-intergranular* cracking mode. At the point marked X in Figure 14A, the thin ferrite phase ribbons, shown by the blue triangular arrows, are not favourably aligned to the crack front, that is, they are aligned at a very high angle, towards the vertical, to the crack front. In this case, the crack will have to advance transgranularly through the grain α_{LR} in front of it. In Figure 14B, the α_{HA} is aligned favourably or lies at low angle to the crack front; hence, the crack advanced following this ferrite ribbon. A similar situation is seen in Figure 14C; however, it appears that the grain of α_{LR} in front of the advancing crack front resisted transgranular propagation of the crack in direction 1 and this caused the nucleation of another crack front that attempted to follow the α_{HA} (shown by the blue arrow) in direction 2. This resulted to crack bifurcation and tends to suggest that the α_{HA} or the α_{LR}/α_{HR} boundary is the preferred path for the crack growth, especially when the boundary is lying at low angle to the crack growth plane. Note that in Figure 14A–C, the α phase dominated the local area with no P phase.

As the ΔK increased, the crack moved into local areas of mixed α and P phases as seen in Figure 14D–K. This region is dominated by the α_{LR} phase and some few P colonies. The α_{HR} is almost absent in this region. It appears that the P is equally likely to cause crack tip diversion and crack branching, but a closer examination showed that these phenomena had been influenced to some extent by the α_{HA}, which appears to serve as the origin or starting phase for the P formation. Figure 14D shows intragranular crack growth and bifurcations; however, one could see that some of the crack tip followed α_{HA} phase. Figure 14E shows the formation of metal crumb and this microstructural region is also dominated by the α_{LR}. Figure 14F–J shows crack branching in the P phase. The tendency for crack branching in the P may be attributed to the orientation of the P colonies and α_{HA} boundaries. In the first case, this tendency may be because the pearlite has two alternating phases—ferrite, α (iron, Fe) and cementite, θ (Fe_3C)[68,69]—with different physical and chemical properties. Daeubler[70] studied the influence of microstructure on the surface FCG behaviour of pearlitic steels and presented a classical case where the P colony orientation influenced the crack growth, especially when the lamellae are favourably oriented to the load axis. In the present study (*PS*), it was observed that α_{LR}/α_{HA} or and α_{HA}/P boundaries are preferred paths of FCG. The blue arrow in Figure 14I shows a branched crack that followed the α_{HA} and the black arrow in Figure 14J shows what appears to be a branched crack front following α_{LR}/P boundary. Figure 14K shows another metal crumb that formed in the vicinity of mainly α_{HR} and α_{LR} phases. It appears that the formation of the metal crumb occurs in the α_{HR} and α_{LR} phase fields as shown in Figure 14E–K.

Figure 15 shows crack path for G8 test in air, under 10 kN, 5 Hz and stress ratio of 0.1, under sinewave. The crack length measured about 10 mm obtained under ΔK of about 18.50 to 34.25 MPa$\sqrt{}$m. The number of high angle diversion and crack branching is by far more in the TMCP steel as compared with low-angle crack tip diversion and crack branching that was consistently found in NR (see Figure 14). Measurements of the angle of crack branching in NR steel show that they are generally below 45°. The only time high-angle diversion was found to be a little above 45° in NR steel is when the crack is avoiding α_{LR} phase or following the α_{HA} or α/P boundaries that is favourably oriented in its path. The α is shown in Figure 15 by the blue triangular arrow. The space enclosed by the red dotted line is the P, whereas the yellow dotted line is the α. Multiple formations of metal crumbs are also shown. These micrographs show that the α_{LR} dominated the microstructure with extensive formation of the α_{HA}. Many of the α_{HA} appear as subgrain phases inside the α_{LR} grains. The presence of α_{HR} is very small and the P nodules are very small also; even some nodules are purely single colonies. The crack path in the TMCP steel is completely non-planar and more complex than that of the NR steel.

It was observed that the crack tip diversion and branching in Figure 15 were caused by the crack tip following path of least resistance created mainly by the α_{HA} or the α_{LR}/α_{HR} boundaries, but mostly by the α_{HA} ribbons. The crack bifurcation is quite extensive with long arms as can be seen in Figure 15A–E, and the diversion of the main active crack front as shown in Figure 15F was measured to be about 43° to the horizontal plane. The branched arms are measured to be in the range 38°–46°. It is interesting to see that the path of least resistant caused many of the branched arms to deviate almost at an angle within this range. This simply implies that both tensile and shear stresses continuously acted on the crack as it propagated in the TMCP, even in the Paris

Region. The metal crumbs as noted in Figure 15 are by far more in the TMCP than the NR steel. It was observed also that the α_{HA} does not only have the potency to divert and branch out crack front, but it can also facilitate rejoining of branched crack fronts into one main crack front, resulting to the crumb formation. This crumb is found to be a tore-off of the steel grain or block of grains. In other words, the fatigue crack front in α–P steel appears not to have a horizontal crack tip edge, but rather series of fluctuating wavelike crack front, whose nature depends on the steel grains and the phases surrounding the grain surfaces. It is important to note that this metal crumb along the crack path has not been reported elsewhere in the literatures or considered in any theoretical formation or treatment. The P colonies in the NR steel are large, blocky and dense. In the TMCP steels, the P appears to grow in two forms—small, blocky colony and a thin, elongated or needle-like morphology colony along what may be described as the α grain boundaries as shown, in some cases, by the space enclosed with the red dotted line in Figure 15. The effect of thermomechanical control rolling process appears to be the disruption of the P banding and blocky morphology into randomly distributed thin P needles. From the observation, it appears that the interface between the α and P is an additional effective preferable path for the crack growth if the P nodule is elongated and aligns favourably to the crack front. In Figure 15, the branched cracks did not just move about linearly but tends to trace the α_{HA} phase. This suggests that the energy needed to propagate through the α_{HA} is much less than that for traversing the α_{LR} grain. The influence of the phase morphology persisted to a length of 9 mm and at 32 MPa$\sqrt{m}$.

The existing theory says that the crack path in Stage II of the da/dN versus ΔK sigmoidal curve is generally across the grains (transgranular)[19] and the material microstructure has little or negligible effect in this region.[3,5,6,20] It can be seen that the crack paths in the NR in Figure 14 and that of TMCP in Figure 15 are not the same. The extensive crack diversion, bifurcation and metal crumbs formation retarded the FCGR and explain why the FCGR in the TMCP is lower than that of the NR in Figure 13. This finding appears to show that microstructure has a strong influence on the rate at which fatigue crack grows in α–P steel in air. This assertion is contrary to the existing theory that microstructure of a steel has little or negligible effect on the FCGR in air. Again, both transgranular and intergranular modes of propagation were observed in air. What appears as the intergranular cracking mode predominated in the TMCP steel. However, what appears as an intergranular mode is actually the growth of the crack through the thin layer of α_{HA} in between the grains of α_{LR} or the P. Hence, this mode is identified here as the *quasi-intergranular* mode. The morphology and chemistry of the microstructural phases and load level appear to determine which mode the crack growth will adopt. Another factor is that the angle the crack front makes with the phases ahead of it tends to determine if it would propagate in transgranular or *quasi-intergranular* mode. However, in Figure 10F, ductile striations were found inside the secondary crack, which actually appears as a branched crack when viewed from the crack line. This clearly shows that the mode is not strictly intergranular, but the crack moved in the α_{HA} phase ribbon immediately adjacent to the α_{LR} or the P interface, justifying the use of the word *quasi-intergranular*. In general, TMCP steel is more resistant to crack propagation than NR steel of the same steel grade. This is made possible by its refined microstructure that branched (with long arms) and diverted the crack front at large angles as compared with the small angle path diversion found in the NR steel. It must be noted that the ability of the α_{HA} to deviate crack front appears to lie in its alloying composition relative to the surrounding phases. The α_{HA} clearly has more of carbon, silicon and oxygen contents than other phases (see Table 3). The increase in the amount of these elements might have embrittled the phase, making it the least resistant path.

5 | FCGRS IN NR AND TMCP S355 STEELS IN SW

A similar study described in Section 3 was carried out in SW. The authors assessed the FCG resistance of J2N, G8 and G10 given in Table 2 in SW. The details of the experimental procedures have been discussed elsewhere.[23,39,43] The experimental results are shown in Figure 16. Three corrosion fatigue crack growth rate (CFCGR) curves, obtained at 12 kN, 9 kN and under 0.3 Hz for the J2N studied by Adedipe et al.,[51] were plotted from the data extracted from a versus N curves. In the present study, one test on the J2N was performed at 9 kN, 0.3 Hz and $R = 0.1$ to validate the results obtained in Adedipe et al.'s study. Mehmanparast et al.[58] studied CFCG in G8 under similar loading conditions and at three different test locations noted as A3, A4; B3, B4; and C3. In identifying the experimental samples, the prefix gives the steel subgrade—J2N, G8 and G10, followed by S (sinewave), P_{max} (maximum load), F (frequency, followed by the frequency value) and the last is the test centre for Mehmanparast et al.'s[58] study. All the tests were performed in SW and under sinewave.

Figure 16A appears to show the partitioning of the FCGRs of NR and TMCP steels in SW into two domains as demarcated by the arbitrary dashed line. The CFCGRs

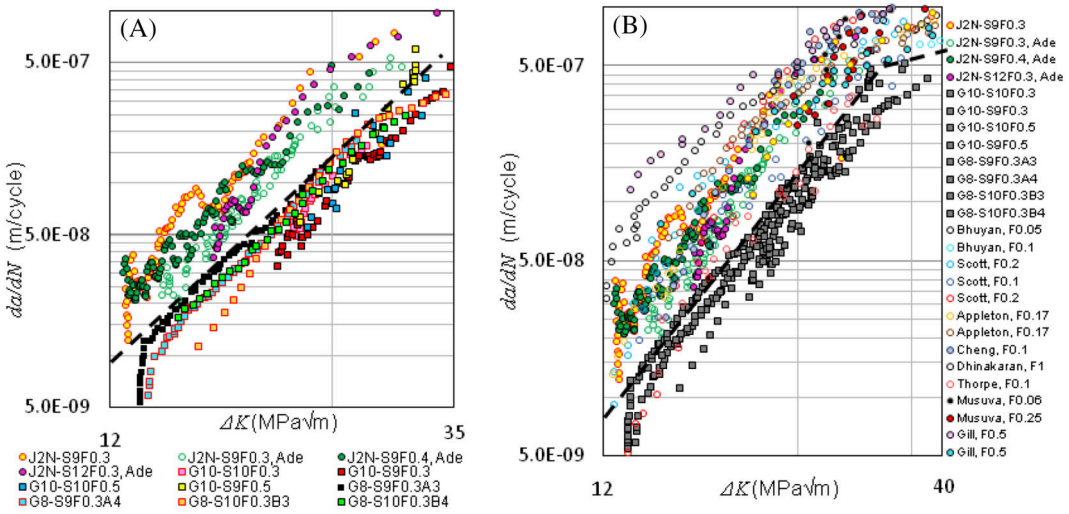

FIGURE 16 (A) Plot of fatigue crack growth rate in seawater normalized rolled and thermomechanical control process steels in the present study and (B) corrosion fatigue crack growth rate curves of α–P steels reported in the literatures [Colour figure can be viewed at wileyonlinelibrary.com]

for the NR steel occupy the upper region of the dashed line and that of the TMCP the lower region. The result of the NR steel tends to show that decreasing the fatigue load level has more accelerating effect than increasing the load as shown by 9 and 12 kN under 0.3 Hz. Selected results for the G8 steel study by Mehmanparast et al.[58] show that increasing the fatigue load level to 10 kN at 0.3 Hz did not necessarily increased the CFCGR above that of 9 kN. In fact, below about 18.50 MPa√m, the CFCGR of the 10 kN decreased below that of 9 kN. For the G10 steels, two load levels (9 and 10 kN) and two frequencies (0.3 Hz and 0.5 Hz) were used. At about 20 MPa√m and above, there is no obvious difference in the CFCGR for the test conditions. In general, the CFCGRs of G10 for all the test conditions were slightly lower than that of G8 and the CFCGRs of all the TMCP subgrades were lower than those of the J2N steel. In fact, the dashed line shows possibly the line of demarcation, though diffused, between the CFCGRs of the NR and TMCP S355 steel subgrades.

In a similar way to air study, the trend found in Figure 16A is validated by carrying out a comparative study of CFCGRs between NR and TMCP α–P steels reported in the literature. The steel grades and mechanical properties of the steels compared with the CFCGR data in the present study are shown in Table 7. It must be mentioned that there are limited studies on the corrosion fatigue of marine steels under the conditions listed in Table 7. Figure 16B presents the CFCGR studies on the steels listed in Table 7. A large separation in the CFGCRs between the NR and TMCP steel is once again observed. It can be observed from Table 7 and Figure 16B that CFCGRs of even some studies carried out at low stress ratios, such as 0.08 by Musuva,[47] were higher than those of the TMCP in Figure 16B. It is often reported in the literatures that plasticity-induced, roughness-induced and oxide-induced crack closure can cause crack growth retardation. It is pertinent to note that during fatigue, the surface asperities or roughness are caused by the ductile stretching or tearing of the fractured surface. These features are areas of high energy and would corrode very fast if in contact with corrosive environment, leaving a smooth surface or deep contour in the case of plastically deformed regions. Hence, they would not contribute significantly to crack retardation. The only factor that may likely cause retardation is oxide-induced crack closure and the extent may depend on the flow rate of the corroding medium and the stress ratio.

5.1 | Microstructure and FCG path in SW under sinewave

A metallographic study was carried out to assess the cause of the disparity in the FCGRs between NR and TMCP as observed in Figure 16. The fractographs for the NR and TMCP steels in SW are shown in Figure 17. Figure 17A is the fractograph obtained in the present study for J2N and Figure 17B is for the same steel obtained by Adedipe.[67] Figure 17C is the corrosion-fatigued surface of the G10 obtained at about 20 MPa√m and Figure 17D is the common feature of the corrosion-fatigued surface of the same material above about 23 MPa√m. Generally, cleavage cracking was not observed and the failure mode remains by ductile striation, which is typical of the failure

TABLE 7 Experimental conditions for the corrosion fatigue crack growth rate data used in this study

Study by	Steel grade	Wave form	Env.	Frequency (Hz)	*R*	% EL	YS (MPa)	UTS (MPa)
Bhuyan	CSA G40.21M 350 WT	s	SW	0.05	0.1	29	405	513
		p-s	SW	0.1	0.1	29	405	513
Scott[44]	BS4360-50D	p-s	SW	0.2	0.5	32	370	538
		t	SW	0.1	0.5	32	370	538
		n-s	SW	0.2	0.5	32	370	538
Appleton[45]	BS4360-50D	s	SW	0.17	0.5	32	368	508
		t	SW	0.17	0.5	32	368	508
Cheng[54]	ABS grade EH36	s	SW	0.1	0.1	21	350	-
Dhinakaran	C-Mn steel	s	NaCl	1.0	0.5	32	459	530
Thorpe[46]	BS4360-50D	s	SW	0.1	0.0, 0.1	32	370	538
Adedipe et al.[51]	S355J + 2 N	s	SW	0.3, 0.35, 0.4	0.1	20	385	531
Musuva[47]	BS4360-50D	s	3.5% NaCl	0.25	0.08	30	386	560
		s	3.5% NaCl	0.06	0.08	30	386	560
Gill	HSLA (MF-80)	s	3.5% NaCl	0.5	0.67	-	653	742
		s	3.5% NaCl	0.5	0.1	-	653	742
PS	S355G8 + M	s	SW	0.3	0.1	35	447	549
PS	S355G10 + M	s	SW	0.3 and 0.5	0.1	36	447	545
	S355J + 2N	s	SW	0.3, 0.35, 0.4	0.1	20	345	-

Abbreviations: Env.,environment; n-s, negative sawtooth; p-s, positive sawtooth; PS, present study; s, sine; t, triangular; SW, seawater.

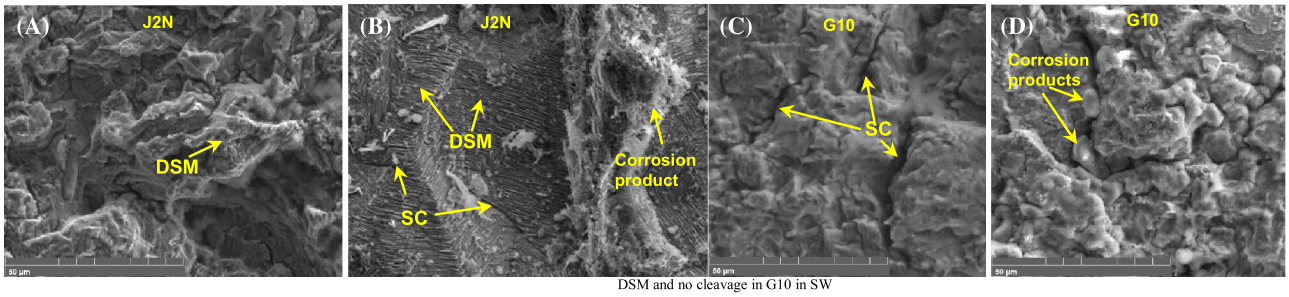

FIGURE 17 Fractographs of fatigued surfaces in seawater for (A, B) J2N and (C, D) G10 [ductile striation mechanism (DSM) with secondary crack (SC) and no cleavage mechanism] [Colour figure can be viewed at wileyonlinelibrary.com]

mechanism in the Paris Region for low-carbon steel. The striations in SW simply appeared to be washed out by the corrosion process and the surfaces were covered by the corrosion products. This washing out progressed with time as can be seen in Figure 17C,D. The secondary cracks in the TMCP steel were larger than that of NR and the corrosion products appear to collect into these secondary cracks over time as seen in Figure 17D.

The collection of the corrosion products into the cracks has the potential of reducing the crack driving force and hence the rate at which the crack is moving. However, the flow of test environment and pumping of the SW in and out of the crack tip as a result of the cyclic action, especially under sinewave, has the capacity of removing corrosion products at the crack tip. Hence, oxide-induced retardation effect may be minimal.

Moreover, crack closure phenomenon is little or negligible in the Paris Region. Because there was no cleavage cracking in the J2N, retardation due to the corrosion product or the oxide-induced crack closure is not sufficient to account for the large difference in CFCGRs in Figure 16. An altervative approach again is to examine the crack path and the microstructural features influencing crack growth in the medium. Figure 18A shows crack path in the G10 material in SW.

Figure 18B is a schematic of Figure 18A. The direction of all the crack growth is from left to right and the direction of applied fatigue force is as given by the yellow double-edge arrow. The crack path was observed for the G10 under sinewave, 9 kN and 0.2 Hz between the ΔK of 19.34 and 30.19 MPa$\sqrt{m}$. The same phenomena of high-angle crack path diversion, multiple crack branching and metal crumbs phenomena characteristic of this TMCP steel in air were also observed in SW (as shown in Figure 18C). However, the number of the branched crack fronts is somewhat less and the extension or length of the branched arm is short compared with that of air. It then appears that the corrosion process had limited the length of the arm of the branched crack through a blunting process. Metal crumbs were also observed, but the extent is small compared with the air test.

Another feature that can be seen is the corrosion attack of the separated surfaces, which resulted to widening of the fatigued surfaces as compared with the test in air (see Figure 11). This widening process may be due to elimination of the small metal crumbs, plastically deformed wake and the *microplastic zone* by the corrosion process. The *microplastic zone*, as used, refers to the closest area(s) to the crack tip that experienced the greatest lattice distortion, stress intensity or plastic deformation as a result of the amplified cyclic force at the crack tip as it opens and closes. These are areas of high lattice energy and are expected to be the points of greatest corrosion rate. Another observation of high importance is that the crack tips of both the main and the branched crack fronts from numbers 1 to 5 are largely sharp as shown by the magnified micrographs of Figure 18C. However, the areas immediately behind the crack tips are widened by the corrosion process as compared with that of the air. It was observed also that the sharpness of the crack tip decreased gradually with increase in the ΔK. It may be that at high ΔK, the crack tip was sufficiently open to allow some degree of blunting by the corrosion process. This generally suggests that the crack tip under 9 kN, 0.2 Hz and sinewave was always sharp up to a particular ΔK, before it started experiencing some significant blunting effect of the corrosion process. Note that

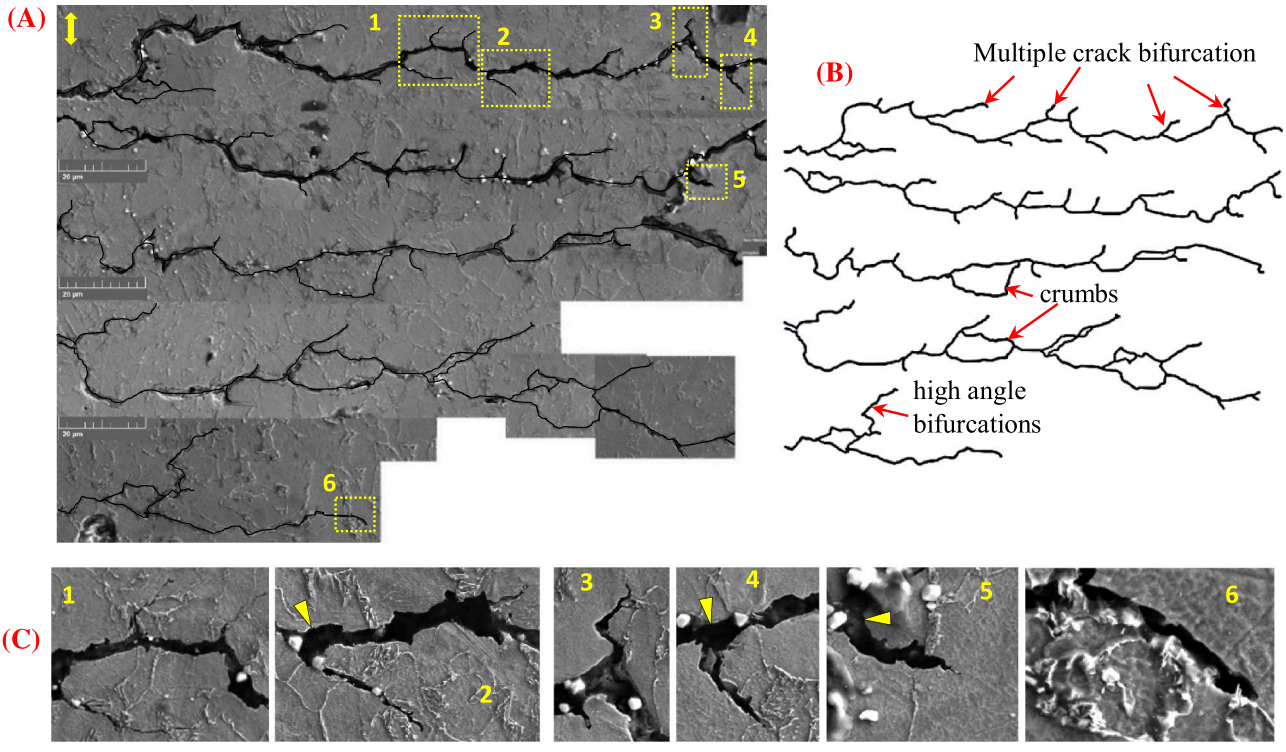

FIGURE 18 (A) Corrosion fatigue crack growth rate path in thermomechanical control process (G10) in seawater: 9 kN, 0.2 Hz, sinewave, crack length between about 22.92 (19.34 MPa$\sqrt{m}$) to 29.70 mm (30.19 MPa$\sqrt{m}$). (B) Schematic of the crack path. (C) Magnification of the crack front (direction: from left to right) [Colour figure can be viewed at wileyonlinelibrary.com]

the sharpness of crack tip ensured that the crack growth was not retarded. The blunting phenomenon may not have much retarding effect at very high ΔK because the crack driving force is enough to continually nucleate sharp crack fronts. In other words, the mechanical fatigue component leads the corrosion process in this domain. This suggests then that at the Paris Region, two domains appear to exist: corrosion-dominated and mechanical fatigue-dominated domains. The corrosion-controlled domain appears to be strongly influenced by the K_{max} and time of crack tip exposure to the corrosive environment.[43]

Figure 19A is a typical nature of the crack path in the J2N steel in SW. Figure 19B is a schematic of Figure 19A. The crack propagated with predominance of low-angle crack tip diversion and very limited low-angle crack branching with the shorter arm in comparison with the TMCP steels. The crack moved on a horizontal plane with minimal zig-zag motion. The crack growth pattern is generally the same with that of air (see Figure 12A) except that the branched arms are shorter and there is widening of the crack gap as a result of the corrosion process. The branched crack tips are relatively blunted, but the main crack tip appeared to maintain its sharpness. No crumb formation was seen, and crack diversion and bifurcation are less than that in air. Hence, one would expect a very high CFCGR for this crack growth pattern if blunting of the main active crack tip did not occur.

In Figure 19, it appears that there is no predominant feature of the phases influencing the crack growth, except that the crack diverted in a zig-zag manner, which is a consequence of the crack propagation mechanism. A closer observation shows some influencing microstructural features. Some of the distinct micrographs showing phases and morphologies influencing the CFCGR for the J2N are presented in Figure 20. However, we could see that the branched crack tips appeared to be following the α/α and α/P interfaces as shown by the arrows. In other words, the preferred crack paths appeared to be the α/α and α/P boundaries. The black arrow is the α/α, whereas the blue arrow is the α/P. In fact, these boundaries are decorated by the ferrite phase ribbon of high alloy content and the crack followed the α_{HA} phase. We can also note the widening activity near and immediately behind the crack tip as it propagated. This is likely to be a result of intense corrosion activity around the *microplastic* zone.

Figure 21 shows the comparison of the FCGR curves for the air and SW tests under sinewave and the experimental conditions are shown in Table 8. Figure 21A shows that CFCGR of 0.2 Hz is higher than that of air by an average factor of 2.5 for the J2N steel. Above about

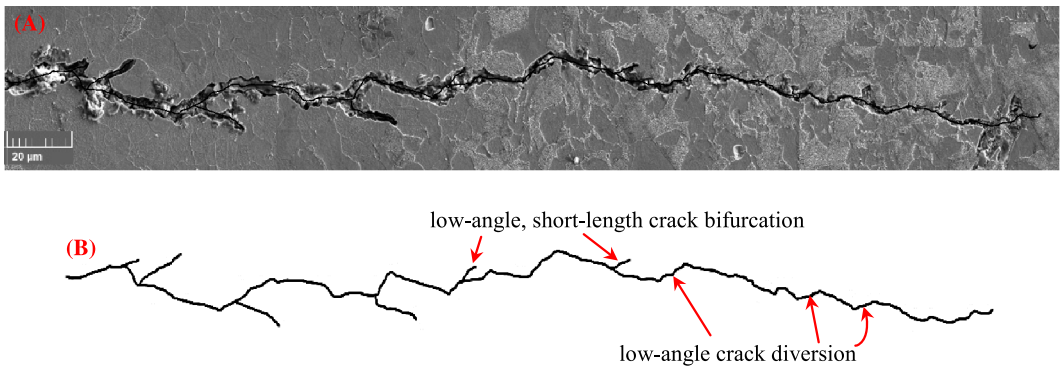

FIGURE 19 (A) Crack path in J2N steel in seawater (10 kN, 0.2 Hz) and (B) schematic of the crack path (direction: from left to right) [Colour figure can be viewed at wileyonlinelibrary.com]

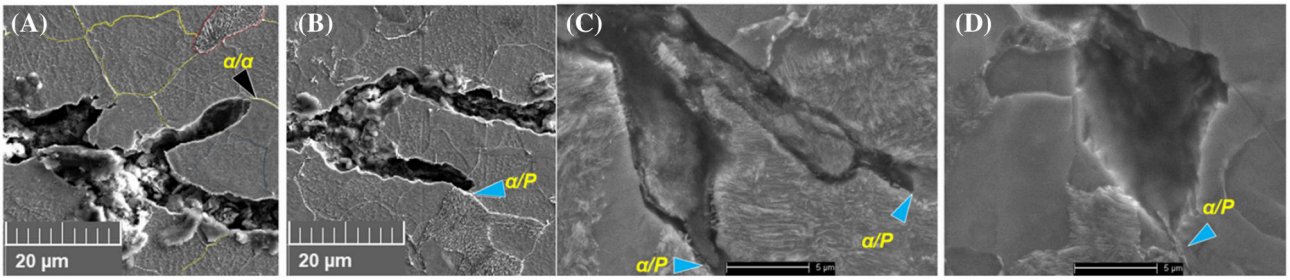

FIGURE 20 Phases influencing fatigue crack growth rate in J2N steel in seawater [Colour figure can be viewed at wileyonlinelibrary.com]

24 MPa√m, the rate increased up to an average factor of 4.0. These values are typical of normalized α–P steels of the same microstructure. The sudden jump in the CFCGR to a factor of about 4 can be explained by examining the crack path in air and SW.

In air (Figure 12), bifurcation, crumb formation and some zig-zag crack propagation were sustained to high ΔK. In the SW, at ΔK above 24 MPa√m, the crumb formation and crack branching were almost absent (Figure 19), and this resulted to a sudden increase in the FCGR to the factor of 4. In Figure 21B, the crack growth rates of the G8 and G10 denoted by the triangular data points, at 10 kN and 5 Hz, are basically the same, confirming that the microstructures are similar. In the Paris Region taken from 19.50 MPa√m, the CFCGR is just higher than that of the air by a factor of about 1.5 measured from their respective mean lines (not shown). There is no obvious trend in the CFCGRs of the three tests in SW under sinewave in Figure 21B. We can reasonably say that the CFCGRs are the same above about 20.50 MPa√m, but below this value, the 9 kN and 0.2 Hz test is somewhat higher. Figure 21C shows the crack growth rates for the two microstructures (J2N and TMCP) in air and SW. It is very clear that the crack path with the least crack diversion, branching and crumb formation gave the highest FCGR. The extent of these three phenomena is a function of the nature of the material microstructure and crack tip condition. If the microstructure, environment and loading condition are such that the three phenomena are extensive, then crack growth retardation occurs; otherwise, the rate may increase. High loading condition in SW tends to limit the extent of crack diversion and branching. This happens as a result of generation of relatively large plastically deformed areas around and ahead of the crack tip by the high loading condition and subsequent rapid dissolution of these areas by the electrochemical process resulting to various degrees of crack tip blunting. An incessant blunting of the crack front will limit the length of the diversion and branched arm, forcing the crack to propagate in a zig-zag amplitude along the horizontal plane. Small zig-zag amplitudes will increase the crack growth rate. This perhaps explains why the crack path found in J2N-A10F5 (Figure 12) and J2N-S10F0.2 (Figure 19) produced the

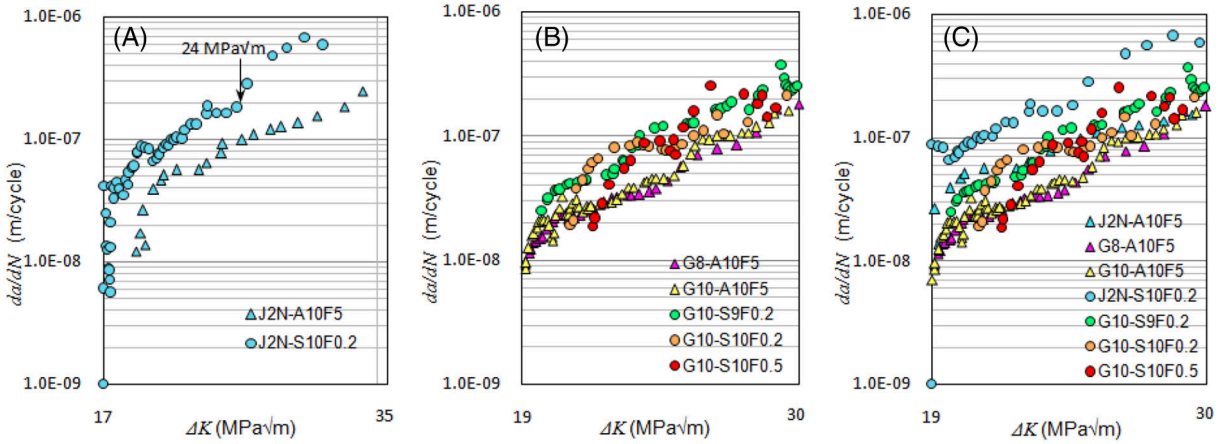

FIGURE 21 Corrosion fatigue crack growth rate in thermomechanical control process and J2N steels at different frequencies under sinewave load [Colour figure can be viewed at wileyonlinelibrary.com]

TABLE 8 Specimen dimensions and loading conditions in air and seawater

#	Test ID	W	B	a_o	a_f	f (Hz)	P_{max} (kN)
1	J2N-A10F5	50.00	16.00	20.50	29.53	5	10
2	J2N-S10F0.2	50.00	16.00	18.32	28.02	0.2	10
3	G8-A10F5	50.15	15.90	20.33	32.12	5	10
4	G10-A10F5	50.01	16.00	20.30	29.53	5	10
5	G10-S9F0.2	50.00	16.00	22.68	30.16	0.2	9
6	G10-S10F0.2	50.00	16.00	21.26	29.11	0.2	10
7	G10-S10F0.5	50.03	16.04	21.20	29.61	0.5	10

Note. In mm, $R = 0.1$.

highest crack propagation rate in air and SW, respectively, as shown in Figure 21C. In general, we observed that the crack path having considerable diversion, bifurcation and crumbs will lower the rate of the crack propagation. In Figure 21C, the CFCGR of the J2N is higher than that of TMCP steel by a factor of about 2.0, and this implies that the microstructure of the TMCP steel is superior to that of J2N in resisting crack growth in α–P steel. Technologically, this implies that the microstructure of steel can be engineered to retard FCG in the Paris Region.

We mentioned earlier that a general stress ratio, $R = 0.1$, has been used in this comparative study. This is an attempt to exclude the effect of the so-called crack closure, as if such effect existed it would affect the steels equally. In fact, the elimination of the asperities or rough edges makes roughness-induced crack closure in corrosive environment unlikely. In the case of interlocking of deviated cracks, in SW, the corrosion process will be rapid in these areas too because the mechanical rubbing action will expose fresh surfaces for fast attack. Thus, the superiority of TMCP steels over the NR in SW, even in air, cannot be attributed to crack closure and is unlikely for interlocking. A plausible reason in this study remains that under stress ratio range of 0.1–0.67, temperature range of 0°C to room temperature and frequency range of 0.05–0.7 Hz, the microstructure of α–P steel strongly affected the rate at which the crack propagated in air and SW in the Paris Region. This study therefore asserts that the existing theory that the microstructure does not significantly affect the Paris Region appears to be incorrect. This tends to be so, when the same grades of steel, but with different phase morphologies, are put into consideration. The major factor responsible for this difference appears to be the ferrite and pearlite phase morphologies and properties, which are functions of the processing method and chemical composition of the steel.

6 | CONCLUSIONS

This study investigated the influence of microstructure on the FCGR in advanced marine steels in the Paris Region, both in air and SW under sinewave fatigue loading. Three phenomena (crack diversion, crack bifurcation and metal crumb formation) were identified as primary factors that retarded crack growth in the steels. The angle of crack tip diversion and bifurcation affected the FCGR. The metal crumb affected FCGR by wedging action. The extent of formation of the three phenomena appears to be a function of the material microstructure, environment and crack tip condition. If the microstructure, environment and loading condition are such that the three phenomena are extensive, then crack growth retardation occurs; otherwise, the rate may increase. That is, decrease in the crack diversion angle, branched crack length and number of metal crumbs formed is found to increase FCGR. High-angle crack tip diversion, bifurcation and reorientation of the metal crumb, resulting to a mismatch or wedging action, retarded FCG. The three factors appear to retard the crack growth by reducing or redistributing the effective stress or driving force at the main active crack tip. In SW, high-angle crack diversion and bifurcation are considerably reduced, and this is a consequence of the repeated crack tip blunting by the electrochemical dissolution process. If the branched crack tips are blunted such that the length is short and the main active crack tip is sharp, CFCGR can increase to about a factor of 4. If the main active crack tip is blunted as well, the crack propagation speed is considerably reduced. *Microplastic* zone appears to control CFCGR in α–P steels. The *microplastic zone* size and the extent of the electrochemical dissolution of the zone (or crack tip blunting) appear to be additional primary factors influencing crack growth. The microstructural phases and morphology local to the main crack front and *microplastic* zone size appear to determine which mode the crack growth will adopt. The angle the crack front makes with the phases ahead of it tends to determine if it would propagate in transgranular or by *quasi-intergranular* mode under low SIFR. This study therefore asserts that the nature of the microstructures of the α–P steels has a strong influence on the FCGR in the Paris Region of the da/dN versus ΔK sigmoidal curve in air and SW. However, considering the relatively small number of tests involved, more experiments are needed to confirm and increase the confidence in the results obtained in this work.

ACKNOWLEDGEMENTS

This work was supported by grant EP/L016303/1 for Cranfield University, University of Oxford and University of Strathclyde Centre for Doctoral Training in Renewable Energy Marine Structures (REMS; http://www.rems-cdt.ac.uk/) from the UK Engineering and Physical Sciences Research Council (EPSRC).

NOMENCLATURE

ao	Initial crack length
CF	Corrosion-fatigue
CFCGR	Corrosion-fatigue crack growth rate
da/dN	Fatigue crack growth rate (m/cycle)
FCG	Fatigue crack growth
FCGR	Fatigue crack growth rate
K	Stress intensity factor (SIF)
LEFM	Linear Elastic Fracture Mechanics

NR	Normalized-rolled
P	Pearlite
Pmax	Maximum load
Pmin	Minimum load
PS	Present study
R	Stress ratio
SIFR	Stress intensity factor range
TMCP	Thermomechanical control process
α	Ferrite
α-P	Ferrite-Pearlite
ΔK	Cyclic SIFR
Δσ	Cyclic stress range
γ	bAustenite
θ	bCementite (Fe3C)
σUTS	Ultimate tensile stress
σy	Yield stress

ORCID

Victor Igwemezie https://orcid.org/0000-0001-5409-0310
Ali Mehmanparast https://orcid.org/0000-0002-7099-7956

REFERENCES

1. ASTM. ASTM E647–15: Standard test method for measurement of fatigue crack growth rates. 2015. Available at: https://doi.org/10.1520/E0647-15.2
2. BSI. BS EN ISO 11782-2:2008: corrosion of metals and alloys—corrosion fatigue testing—part 2: crack propagation testing using precracked specimens. British Standard. 2008.
3. Ritchie RO. Near-threshold fatigue-crack propagation in steels. *Int Metals Rev*. 1979;24(1):205-230.
4. Stonesifer FR. Effect of grain size and temperature on fatigue crack propagation in A533 b steel. *Eng Fract Mech*. 1978;10(2):305-314.
5. Milella PP. *Fatigue and Corrosion in Metals*. Milan: Springer-Verlag; 2013:529-530.
6. Zerbst U, Madia M, Vormwald M, Beier HT. Fatigue strength and fracture mechanics—a general perspective. *Eng Fract Mech Elsevier Ltd*. 2018;198:2-23.
7. Chen DL, Wang ZG, Jiang XX, Ai SH, Shih CH. The dependence of near-threshold fatigue crack growth on microstructure and environment in dual-phase steels. *Mater Sci Eng A*. 1989;108(C):141-151.
8. Liaw PK. Mechanisms of near-threshold fatigue crack growth in a low alloy steel. *Acta Metall*. 1985;33(8):1489-1502.
9. Jacob A, Mehmanparast A, D'Urzo R, Kelleher J. Experimental and numerical investigation of residual stress effects on fatigue crack growth behaviour of S355 steel weldments. *Int J Fatigue*. 2019;128(105196).
10. Jacob A, Oliveira J, Mehmanparast A, Hosseinzadeh F, Kelleher J, Berto F. Residual stress measurements in offshore wind monopile weldments using neutron diffraction technique and contour method. *Theor Appl Fract Mech*. 2018;96(April):418-427.
11. Zerbst U, Vormwald M, Pippan R, Gänser H-P, Sarrazin-Baudoux C, Madia M. About the fatigue crack propagation threshold of metals as a design criterion—a review. *Eng Fract Mech*. 2016;153(November 2014):190-243.
12. Ritchie RO. Mechanisms of fatigue-crack propagation in ductile and brittle solids. *Int J Fatigue*. 1999;100:55-83.
13. Thompson AW, Bucci RJ. The dependence of fatigue crack growth rate on grain size. *Metall Trans*. 1973;4(4):1173-1175.
14. Lindigkeit J, Terlinde G, Gysler A, Lutjering G. The effect of grain size on the fatigue crack-propagation behavior of age-hardened alloys in inert and corrosive environment. *Acta Metall*. 1979;27(11):1717-1726.
15. Hoeppner DW. The effect of grain size on fatigue crack growth in copper. Fatigue Crack Propagation, ASTM 415. 1967;18(STP415-EB/Jun): 489.
16. Francois D. The influence of the microstructure on fatigue. In: Branco CM, Rosa LG, eds. NATO ASI S*Advances in Fatigue Science and Technology*; 1989. https://doi.org/10.1016/B978-0-12-374364-0.50017-5
17. Laird C, Smith GC. Crack propagation in high stress fatigue. *Philos Mag*. 1962;7(77):847-857.
18. Pelloux RMN. Crack extension by alternating shear. *Eng Fract Mech*. 1970;1(4):697-700.
19. Stephens RI, Fatemi A, Stephens RR, Fuchs HO. *Metal Fatigue in Engineering*. 2nd ed. NY: John Wiley & Sons; 2001:51.
20. Krupp U. *Fatigue Crack Propagation in Metals and Alloys: Microstructural Aspects and Modelling Concepts*. WILEY-VCH Verlag GmbH & Co: Weinheim; 2007 136 p.
21. Elber W. Fatigue crack closure under cyclic tension. *Eng Fract Mech*. 1970;2:37-45.
22. Elber W. The significance of fatigue crack closure. ASTM STP 486 - Damage Tolerance in Aircraft Structures. 1971: 230–242.
23. Igwemezie V, Mehmanparast A, Kolios A. Materials selection for XL wind turbine support structures: a corrosion-fatigue perspective. *Mar Struct Elsevier*. 2018;61:381-397.
24. Steel International T. New horizons—supply solutions in offshore structual steel. 2010. Available at: http://www.tatasteeleurope.com/static_files/StaticFiles/Business_Units/International/TataSteelInternationalOffshoreCapability2010.pdf (Accessed: 5 April 2016).
25. Corus Construction & Industrial. European structural steel standard EN 10025: 2004. 2004. Available at: http://www.tf.uni-kiel.de/matwis/amat/iss/kap_9/articles/en_steel_standards.pdf (Accessed: 5 April 2016)
26. Tata Steel. Advance sections. 2013. Available at: http://www.tatasteeleurope.com/file_source/StaticFiles/section_plates_publications/sections_publications/AdvancetoEurocodeSept13.pdf
27. Parker Steel Company. S355 EN 10025: standard structural steel products. 2012. Available at: http://www.metricmetal.com/products/GradeDescriptions/S355GradeDescription.php (Accessed: 1 April 2016)
28. Dillinger. Thermomechanically rolled fine-grained steels. 2016. Available at: https://www.dillinger.de/d/en/products/heavyplate/thermomechanically-finegrained/ (Accessed: 11 April 2016)
29. Mehmanparast A, Taylor J, Brennan F, Tavares I. Experimental investigation of mechanical and fracture properties of offshore wind monopile weldments: SLIC interlaboratory test results. *Fatigue Fract Eng Mater Struct*. 2018;41(12):2485-2501.
30. Igwemezie V, Mehmanparast A, Kolios A. Current trend in offshore wind energy sector and material requirements for

fatigue resistance improvement in large wind turbine support structures—a review. *Renew Sustain Energy Rev*. 2019;101:181–196.

31. De Meester B. The weldability of modern structural TMCP steels. *ISIJ Int*. 1997;37(6):537-551.
32. Tamura I, Sekind H, Taanaka T, Ouchi C. *Thermomechanical processing of high-strength low-alloy steels*. Bodmin, Cornwall: Butterworth & Co; 1988 248 p.
33. Bhadeshia HKDH. Bainite in steels—transformation, microstructure and properties. 2nd edn. Cambridge, UK: IOM Communications; 2001.
34. GRANGE RA. Fundamentals of deformation processing: proceedings. In: Backofen WA (ed.) Volume 9 of Sagamore Army Materials Research Conference proceedings. Syracuse University Press; 229. Available at: https://books.google.co.uk/books/about/Fundamentals_of_deformation_processing.html?id=QOg_AQAAIAAJ&redir_esc=y (Accessed: 17 December 2018)
35. Fukumoto Y. New constructional steels and structural stability. *Eng Struct*. Elsevier. 1 October 1996;18(10):786-791.
36. Shikanai N, Mitao S, Endo S. Recent development in microstructural control technologies through the thermo-mechanical control process (TMCP) with JFE steel's high-performance plates. 2008. Available at: http://www.jfe-steel.co.jp/en/research/report/011/pdf/011-02.pdf (Accessed: 17 December 2018)
37. Bhadeshia HKDH. Interpretation of the microstructure of steels. Phase transformation group, University of Cambridge Available at: http://www.phase-trans.msm.cam.ac.uk/2008/Steel_Microstructure/SM.html (Accessed: 9 October 2018)
38. Igwemezie VC, Ovri JEO. Investigation into the effects of microstructure on the corrosion susceptibility of medium carbon steel. *Int J Eng Sci (IJES)*. 2013;2(6):11-26.
39. Igwemezie V, Dirisu P, Mehmanparast A. Critical assessment of the fatigue crack growth rate sensitivity to material microstructure in ferrite–pearlite steels in air and marine environment. *Mater Sci Eng A*. 2019;754:750-765.
40. Slezak T, Sniezek L. A comparative LCF study of S960QL high strength steel and S355J2 mild steel. *Proc Eng*. 2015;114:78-85.
41. Steimbreger C. Fatigue of Welded Structures—Master Thesis. Lulea University of Technology; 2014.
42. Korda AA, Mutoh Y, Miyashita Y, Sadasue T, Mannan SL. In situ observation of fatigue crack retardation in banded ferrite–pearlite microstructure due to crack branching. *Scr Mater*. 2006;54(11):1835-1840.
43. Igwemezie V, Mehmanparast A. Waveform and frequency effects on corrosion-fatigue crack growth behaviour in modern marine steels. *Int J Fatigue*. 2020;134:105484. https://doi.org/10.1016/j.ijfatigue.2020.105484
44. Scott PM, Thorpe TW, Silvester DRV. Rate-determining processes for corrosion fatigue crack growth in ferritic steels in seawater. *Corros Sci*. 1983;23(6):559-575.
45. Appleton RJ. Corrosion Fatigue of a C–Mn Steel, PhD Thesis. Department of Mechanical Engineering, University of Glasgow; 1985. Available at: http://theses.gla.ac.uk/2176/ (Accessed: 13 February 2018)
46. Thorpe TW, Scott PM, Rance A, Silvester D. Corrosion fatigue of BS4360:50D structural-steel in seawater. *Int J Fatigue*. 1983;5(3):123-133.
47. Musuva JK. PhD Thesis—Fatigue Crack Growth in a Low-Alloy Steel. University of London; 1980. Available at: https://spiral.imperial.ac.uk/bitstream/10044/1/35278/2/Musuva-JK-1980-PhD-Thesis.pdf (Accessed: 27 September 2018)
48. Thompson JWC. PhD Thesis—Phenomenological Investigation of the Influence of Cathodic Protection on Corrosion Fatigue Crack Propagation Behaviour, in a BS 4360 50D type structural steel and associated weldment microstructures, in a marine environment. Cranfield University; 1984.
49. Correia JAFO, Blasón S, De Jesus AMP, Canteli AF, Moreira PMGP, Tavares PJ. Fatigue life prediction based on an equivalent initial flaw size approach and a new normalized fatigue crack growth model. *Eng Fail Anal*. 2016;69:15-28.
50. De Jesus AMP, Matos R, Fontoura BFC, Rebelo C, Simões Da Silva L, Veljkovic M. A comparison of the fatigue behavior between S355 and S690 steel grades. *J Constr Steel Res*. Elsevier Ltd. 2012;79(August):140-150.
51. Adedipe O, Brennan F, Kolios A. Corrosion fatigue load frequency sensitivity analysis. *Mar Struct Elsevier Ltd*. 2015;42:115-136.
52. Xiong Y, Hu XX. The effect of microstructures on fatigue crack growth in Q345 steel welded joint. *Fatigue Fract Eng Mater Struct*. 2012;35(6):500-512.
53. Laurito DF, Baptista CARP, Torres MAS, Abdalla AJ. Microstructural effects on fatigue crack growth behavior of a microalloyed steel. *Proc Eng Elsevier*. 2010;2(1):1915-1925.
54. Cheng YW. The fatigue crack growth of a ship steel in seawater under spectrum loading. *Int J Fatigue*. 1985;7(2):95-100.
55. Callister DR. A study of fatigue crack propagation in quenched and tempered and controlled roller HSLA steels. Cranfield Institute of Technology; 1987.
56. Tsay LW, Chern TS, Gau CY, Yang JR. Microstructures and fatigue crack growth of EH36 TMCP steel weldments. *Int J Fatigue*. 1999;21(8):857-864.
57. Chapetti MD, Miyata H, Tagawa T, Miyata T, Fujioka M. Fatigue crack propagation behaviour in ultra-fine grained low carbon steel. *Int J Fatigue*. 2005;27(3):235-243.
58. Mehmanparast A, Brennan F, Tavares I. Fatigue crack growth rates for offshore wind monopile weldments in air and seawater: SLIC inter-laboratory test results. *Mater Des*. 2017;114:494-504.
59. Tavares I, Brennan F. The SLIC Project. 2015. Available at: http://www.ewea.org/offshore2015/conference/allposters/PO081.pdf
60. Atkinson JD, Lindley TC. Effect of stress waveform and hold-time on environmentally assisted fatigue crack propagation in C–Mn structural steel. *Metal Sci*. 1979;13(7):444-448.
61. Achilles RD, Bulloch JH. The influence of waveform on the fatigue crack growth behaviour of SA508 cl III RPV steel in various environments. *Int J Pres Ves Pip*. 1987;30(5):375-389.
62. Barsom JM, Rolfe ST. *Fracture and Fatigue Control in Structures: Applications of Fracture Mechanics* 3rd ed. West Conshohocken: ASTM; 1999:318-323.
63. Barsom JM. Corrosion-fatigue crack propagation below KIscc. *Eng Fract Mech*. 1971;3(1):15-25.
64. Musuva JK, Radon JC. The effect of stress ratio and frequency on fatigue crack growth. *Fatig Eng Mater Struct*. 1979;1(4):457-470.

65. Li X, Cao L, Wang M, Du F. Groove design and microstructure research of ultra-fine grain bar rolling. Modeling and numerical simulation of material science. Scientific Research Publishing; 22 October 2012; 02(04): 67–75.
66. Saeed-Akbari A. Determination of steels microstructural components based on novel characterisation techniques. RWTH Aachen; 2008. Available at: https://doi.org/10.1007/BF03192151
67. Adedipe O. *PhD theses - Integrity of offshore structures*. United Kingdom: Cranfield University; 2015.
68. Kavishe FPL, Baker TJ. Effect of prior austenite grain size and pearlite interlamellar spacing on strength and fracture toughness of a eutectoid rail steel. *Mater Sci Technol*. 1986;2(8): 816-822.
69. Callister WDJ. *Materials Science and Engineering An Introduction*. 7th ed. USA: John Wiley & Sons, Inc; 2007:226-227.
70. Daeubler MA, Thompson AW, Bernstein IM. Influence of microstructure on fatigue behavior and surface fatigue crack growth of fully pearlitic steels. *Metall Trans A*. 1990;21A: 925-932.

How to cite this article: Igwemezie V, Mehmanparast A, Brennan F. The influence of microstructure on the fatigue crack growth rate in marine steels in the Paris Region. *Fatigue Fract Eng Mater Struct*. 2020;43:2416–2440. https://doi.org/10.1111/ffe.13312